

Exploring Regional Climate of the Euro-Mediterranean Using a Variable-Resolution Configuration of the Global Community Earth System Model (VR-CESM)

Burcu Boza¹, Adam R Herrington², Mehmet Ilicak¹, Gokhan Danabasoglu³, and Omer Lutfi Sen¹

¹Istanbul Technical University

²National Center for Atmospheric Research

³National Center for Atmospheric Research (NCAR)

April 16, 2024

Abstract

A Variable-Resolution, global configuration of the Community Earth System Model (VR-CESM) in which the atmosphere and land are the only active components is employed to investigate the climate of the Euro-Mediterranean region. Two variable-resolution grids with regionally-refined resolutions of 0.25° and 0.125° over the study domain, respectively, are used. The fidelity of these VR-CESM simulations is evaluated considering the near-surface air temperature and precipitation fields for the 2000-2014 period in comparison to available observation-based datasets and those of a coarse resolution (quasi-uniform 1°) control simulation. Our analysis shows that, as a global model, VR-CESM is a promising alternative to regional climate models to advance our understanding of the Euro-Mediterranean climate. The improvements obtained are mainly related to a better representation of the complex topography of the region with higher resolution. Increasing the regional resolution to 0.25° generally yields considerable improvements over the control simulation, however some persistent biases remain. Doubling the highest resolution to 0.125° leads to only modest improvements, primarily in the representation of small-scale processes including representation of extreme events that are of substantial relevance for the present and future of the regional climate.

Hosted file

BozaBurcu_2024_ExploringRegClim.docx available at <https://authorea.com/users/764356/articles/742308-exploring-regional-climate-of-the-euro-mediterranean-using-a-variable-resolution-configuration-of-the-global-community-earth-system-model-vr-cesm>

Hosted file

BozaBurcu_2024_supplement.docx available at <https://authorea.com/users/764356/articles/742308-exploring-regional-climate-of-the-euro-mediterranean-using-a-variable-resolution-configuration-of-the-global-community-earth-system-model-vr-cesm>

31 **Abstract**

32 A Variable-Resolution, global configuration of the Community Earth System Model (VR-
33 CESM) in which the atmosphere and land are the only active components is employed to
34 investigate the climate of the Euro-Mediterranean region. Two variable-resolution grids with
35 regionally-refined resolutions of 0.25° and 0.125° over the study domain, respectively, are used.
36 The fidelity of these VR-CESM simulations is evaluated considering the near-surface air
37 temperature and precipitation fields for the 2000-2014 period in comparison to available
38 observation-based datasets and those of a coarse resolution (quasi-uniform 1°) control
39 simulation. Our analysis shows that, as a global model, VR-CESM is a promising alternative to
40 regional climate models to advance our understanding of the Euro-Mediterranean climate. The
41 improvements obtained are mainly related to a better representation of the complex topography
42 of the region with higher resolution. Increasing the regional resolution to 0.25° generally yields
43 considerable improvements over the control simulation, however some persistent biases remain.
44 Doubling the highest resolution to 0.125° leads to only modest improvements, primarily in the
45 representation of small-scale processes including representation of extreme events that are of
46 substantial relevance for the present and future of the regional climate.

47

48 **Plain Language Summary**

49 The Euro-Mediterranean region has a highly complex and distinctive climatology making the
50 simulation of the regional climate a challenging task. The region is influenced by several large-
51 scale circulation patterns, requiring a global modeling framework. At the same time, due to its
52 rather complex topography, models need high spatial resolution to represent many small-scale
53 climatic features of the region. To address this challenge, we employ a variable-resolution
54 configuration of the Community Earth System Model (VR-CESM) with a high resolution over
55 this region within a global model which has lower resolution elsewhere. We show that VR-
56 CESM simulations produce better representations of precipitation and surface temperature,
57 especially over complex topography, in comparison to a control simulation with no resolution
58 enhancement over the region.

59

60 **1 Introduction**

61 The Euro-Mediterranean region lies in a transitional zone between arid and subarctic
62 climates, mainly including arid, Mediterranean, oceanic and humid continental climates (Kottek
63 et al., 2006). It is influenced by large-scale circulation patterns such as the Icelandic Low, the
64 Siberian High, the Azores High, and the South Asian Monsoon as well as by teleconnection
65 patterns such as the El Niño Southern Oscillation and the Arctic Oscillation, among others (Sen
66 et al., 2019). The climate of the Mediterranean Basin is characterized by high seasonality as it
67 has a typical winter maximum in precipitation, in contrast with humid climate of Europe, which
68 features rainy conditions all year around. The presence of inland seas, land-sea contrast, complex
69 topography, and coastlines of the region all have a strong modulating effect on large-scale
70 patterns leading to many meso-beta scale climatic features locally. The region contains two large
71 semi-enclosed seas: the Mediterranean Sea and the Black Sea – the former with a connection to
72 the Atlantic Ocean through the narrow Gibraltar Strait. Together with the surrounding high
73 mountain chains, these two seas create sharp land-sea contrasts. The Mediterranean Sea is, in
74 particular, a major source of heat and moisture for the surrounding areas, and it is large enough
75 to host both subtropical cyclones and tropical-like cyclones called the medicanes (Fita et al.,
76 2007). For detailed information on the main characteristics of the regional climate and the spatial
77 patterns of seasonal precipitation and surface temperature, the reader is referred to Lionello et al.
78 (2006) and Xoplaki (2002), respectively.

79 The Mediterranean Basin is a climate change hotspot (Giorgi, 2006) with a projected
80 regional warming above global means and reduced rainfall. These projected warmer and drier
81 conditions threaten human population and ecosystems in the region. Highly interconnected
82 climate risks include water scarcity, water and food security, risks related to droughts, floods,
83 heat waves and wildfires, and ecosystem losses. The Euro-Mediterranean region is frequently
84 affected by extreme climate events such as heat waves, cold spells, heavy precipitation, and
85 windstorms, and these events are generally projected to intensify, become more frequent and
86 longer in the future. These vulnerabilities of the region add to the importance and urgency of
87 better understanding the mesoscale and large-scale dynamics that determine the regional present-
88 day climate. Considering their large-scale links (Bozkurt et al., 2019; Insua-Costa et al., 2022;
89 Toreti et al., 2010), taking a global perspective is even more important for extreme events.

90 With its unique characteristics, modeling the Euro-Mediterranean region's climate is a
91 challenging task. Reliable and robust simulations with an adequate spatiotemporal resolution to
92 resolve sharp regional gradients (Onol & Semazzi, 2009), such as the precipitation and
93 temperature differences occurring over short distances due to the region's mountainous
94 topography, are needed. At the same time, model simulations are expected to adequately
95 represent global and regional teleconnections, large-scale circulation patterns, and multi-scale
96 interactions driving the regional climate. Uniform high-resolution (0.1° - 0.25°) general
97 circulation models (GCMs) could be used to address these challenges (e.g., Small et al., 2014),
98 but their routine use would be prohibitively expensive due to substantial computational costs.

99 An alternative is to employ downscaling with high-resolution regional climate models
100 (RCMs). While RCMs allow region-specific tunings to simulate regional climates more
101 realistically, which is not possible with GCMs (Gutowski et al., 2020; Mauritsen et al., 2012),
102 they employ boundary conditions from other global models or reanalysis products, and thus
103 inherit biases from those, and more importantly, they generally lack two-way interactions
104 (Lionello et al., 2006; Raisanen et al., 2004; Rummukainen, 2015). Both of these issues can lead

105 to inconsistencies between the global and regional scales which can be exacerbated by use of
106 different parameterizations in the global and regional models (Chen, 2002; Ringler et al., 2011;
107 Wang et al., 2004). Indeed, these challenges have been identified in studies that investigated the
108 climate of the Euro-Mediterranean region with RCMs (e.g., Kotlarski et al., 2014). For example,
109 Bergant et al. (2007) investigated the systematic errors in the simulation of the European climate
110 with the Abdus Salam International Centre for Theoretical Physics Regional Climate Model
111 version 3 (ICTP-RegCM3) driven by the reanalysis product from the National Centers for
112 Environmental Prediction (NCEP) and NCAR (NCEP/NCAR reanalysis), and found that most of
113 the systematic errors in the RegCM3 simulation can be related to boundary conditions. They also
114 reported that RCMs cannot correct the biases in the data that they are driven by, but only add
115 regional details to the large-scale information (Fan et al., 2014; Feser et al., 2011). In another
116 study, Onol and Semazzi (2009) investigated the potential role of global warming in modulating
117 the future climate over the eastern Mediterranean region by also employing ICTP-RegCM3 to
118 downscale the present and future climate scenario simulations generated by the National
119 Aeronautics and Space Administration's (NASA) finite-volume atmospheric GCM (fvGCM).
120 They pointed out that the drier summer conditions simulated by the model were inherited by
121 RegCM3 through the lateral boundary conditions from the fvGCM simulation, which was also
122 very dry during summers. The study also found a high level of agreement between the RegCM3
123 and fvGCM circulation changes. While this finding indicates that the distortion of flow across
124 the lateral boundaries is rather small – a positive aspect for regional model configuration, it
125 emphasizes that RCMs inherit features of boundary conditions from GCMs. Another example is
126 provided by Bozkurt et al. (2012) which downscaled the outputs of three GCMs and a reanalysis
127 dataset using RegCM3 to assess the capability of the regional model in simulating the present-
128 day climatology of the eastern Mediterranean – Black Sea region. In their study, they, too,
129 highlighted the propagation of the GCM features to the large-scale fields generated by the RCM
130 simulation.

131 Variable-resolution (VR) models, which allow regional refinement within a global
132 framework, offer a promising alternative to other fine-resolution modeling approaches discussed
133 above for investigating regional climates and can be thought of as a bridge between the costly
134 uniform high-resolution models and regional models with their challenges. Indeed, the
135 Community Earth System Model (CESM) provides such an option with its VR atmosphere and
136 land components denoted as VR-CESM. It can be configured easily to increase model resolution
137 in regions of interest. To date, VR-CESM has been successfully used in various studies that
138 include investigations of the orographic forcing and snowpack in Sierra Nevada (Rhoades et al.,
139 2015), Greenland ice sheet surface mass balance (van Kampenhout et al., 2019), wind speed in
140 California (Wang et al., 2020), tropical cyclones (Reed et al., 2012; Zarzycki, Jablonowski, &
141 Taylor, 2014), mean climatology of near-surface temperature and precipitation over California
142 (Huang et al., 2016), climate of the Tibetan Plateau (Rahimi et al., 2019), and atmospheric rivers
143 (Rhoades et al., 2020).

144 In this paper, we present the very first application of VR-CESM to study the present-day
145 climate over the Euro-Mediterranean region. The fidelity of the simulations will be evaluated
146 considering primarily the near-surface (2-m) air temperature and precipitation fields for the
147 2000-2014 period against available observation-based datasets, as they are essential variables for
148 describing climate, have direct impacts on human and ecosystems, and are important indicators
149 for climate change. The performance of the fine resolution refinement will be compared to that
150 of a coarse resolution (quasi-uniform 1°) control simulation across daily, monthly, seasonal, and

151 annual time scales. We also explore the representation of extreme maximum temperature and
152 precipitation with high resolution, motivated by the known skill of high spatiotemporal
153 resolution in simulating such extreme events more realistically (Gutowski et al., 2020) and by the
154 ability of VR-CESM in reproducing extreme statistics from high-resolution simulations
155 (Gettelman et al., 2018). We also present findings from a parameter tuning experiment we
156 carried out to investigate how calibration of some cloud radiative parameters influences the
157 representation of longwave- and shortwave-cloud forcings.

158 The manuscript is organized as follows. In section 2, the model and methodology along
159 with evaluation datasets are provided. Section 3 is devoted to the presentation and interpretation
160 of results, followed by section 4 that summarizes our findings and conclusions.

161 **2 Model and Evaluation Methodology**

162 **2.1 Model**

163 CESM is a fully coupled global Earth system model developed and maintained by the
164 National Science Foundation National Center for Atmospheric Research (NSF NCAR) with
165 contributions from many researchers from universities and other institutions
166 (<https://www.cesm.ucar.edu/models/cesm2/>). In this study, CESM2.2 version is used
167 (Danabasoglu et al., 2020) in its Atmospheric Model Intercomparison Project (AMIP) setup in
168 which the Community Atmosphere Model version 6.3 (CAM6; Bogenschutz et al., 2018;
169 Gettelman et al., 2019) is the atmosphere component and the Community Land Model version 5
170 (CLM5; Lawrence et al., 2019) with satellite phenology is the land component. This AMIP
171 configuration is run with prescribed historical sea surface temperatures (SSTs) and sea ice
172 concentrations rather than active ocean and sea-ice components (even so, the sea-ice component,
173 CICE (Hunke et al., 2015), uses a prognostic thermodynamic model). The merged Hadley-OI,
174 based on the monthly-mean Hadley Centre sea ice and SST dataset version 1 (HadISST1) and
175 version 2 of the National Oceanic and Atmospheric Administration (NOAA) weekly optimum
176 interpolation (OI) SST analysis, is used as the surface boundary forcing dataset (Hurrell
177 et al., 2008).

178 CAM6 employs the unified turbulence scheme, Cloud Layers Unified by Binormals
179 (CLUBB; Golaz et al. 2002; Larson, 2017), which is a prognostic moist turbulence scheme, and
180 an improved two-moment prognostic cloud microphysics, the Morrison and Gettelman
181 microphysics scheme version 2 (MG2; Gettelman & Morrison, 2015). Prognostic rainfall and
182 snowfall capability of the MG2 scheme substantially improves accuracy of mountainous
183 hydroclimate simulations at grid-spacings of < 28 km (Rhoades et al., 2018) where fallout
184 duration of hydrometeors is longer than that of horizontal transport duration across the model
185 grid (Rahimi et al., 2019). The model uses hybrid sigma coordinates with 32 terrain-following
186 vertical levels. The lowest model level is at approximately 60 m, and top of the model is at 3.64
187 hPa (~ 40 km).

188 We employ the Spectral Element dynamical core option (CAM-SE) of CAM6. This
189 hydrostatic dynamical core, which offers VR functionality, is available as an out-of-the-box
190 feature for the first time in CESM2.2. It has many attractive accuracy and conservation features
191 for high-resolution and VR applications, allowing regional dynamical downscaling (or regional
192 grid refinement) within a global context. Here, we briefly present some of these and refer to
193 Dennis et al. (2012), Lauritzen et al. (2018), and Taylor and Fournier (2010) for further details.

194 Spectral element method, which is designed for unstructured grids, offers geometric
195 flexibility of finite element methods and high-order accuracy and mesh convergence properties
196 of spectral methods (Dennis et al., 2012). CAM-SE is based on nonoverlapping quasi-uniform
197 grids (spectral elements). Therefore, numerical instability arising from polar convergence of
198 meridians in traditional latitude-longitude (finite-volume) grids, the so-called ‘pole problem’, is
199 not an issue (Herrington et al., 2022). In CAM-SE, the primitive equations of motion are solved
200 on individual elements. Hence, CAM-SE is a highly scalable dynamical core and well suited for
201 high-resolution simulations by utilizing today’s parallel computing opportunities. It uses dry-
202 mass hybrid vertical coordinates which simplifies the representation of mass effects of moisture
203 and condensates in thermodynamic and momentum equations, that is, in the dynamical core,
204 which is also particularly important in high resolutions (Bacmeister et al., 2012). Such dry-mass
205 vertical coordinates offer consistent coupling with physical parametrizations and better treatment
206 of total energy conservation (Lauritzen et al., 2018).

207 In CAM-SE, a fourth-order hyper-viscosity is applied for horizontal diffusion (Dennis et
208 al., 2012). Tensor hyper-viscosity, a mechanism for the dissipation of grid scale variance of
209 multi-resolution grids, is only active in VR configurations (Guba et al., 2014). Tensor hyper-
210 viscosity coefficients scale independently for both length scales of quadrilateral elements instead
211 of using a constant coefficient based on a single length scale. This leads to a smoother transition
212 between different resolutions and avoids artifacts in the transition regions.

213 VR-CESM takes advantage of CAM-SE’s increased grid flexibility (Zarzycki,
214 Jablonowski, & Taylor, 2014). With the ability of using unstructured grids, VR-CESM allows
215 grid refinement by smooth transition from coarse to high resolution thus preserving far-field
216 resolution and eliminating the corresponding drawback of grid-stretching techniques (Rahimi et
217 al., 2019; Wu et al., 2017). In such techniques, which are extensively used in VR
218 configurations (Abiodun et al., 2008; Fox-Rabinovitz et al., 2006; McGregor & Dix 2008;
219 Tomita, 2008), a gradually coarsening mesh as going away from the refined region degrades the
220 representation of large-scale circulations, because the degrees-of-freedom is held constant while
221 decreasing the horizontal resolution away from the refined region. Whereas in VR-CESM,
222 degrees-of-freedom are added to make a statically-refined region (Zarzycki, Levy, et al., 2014),
223 increasing the accuracy at the far-field.

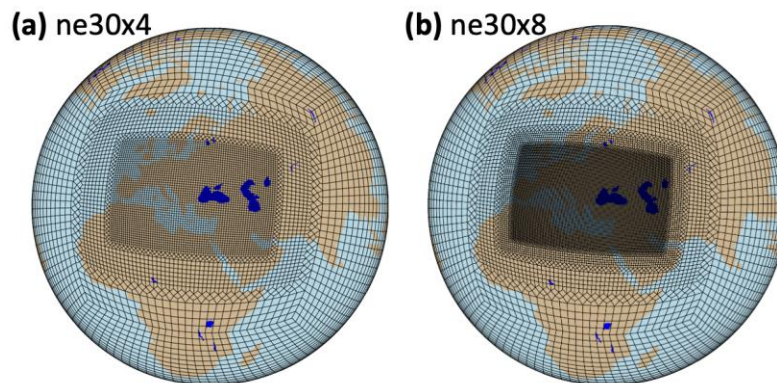
224 2.1.1 Grids

225 VR grids used in this study were developed employing the C++ based open-source
226 software package SQuadGen (Guba et al., 2014; Ullrich, 2014). These are cubed-sphere grids
227 consisting of quadrilateral unstructured meshes obtained by gnomonic equal-angle projection of an
228 inscribed cube onto a sphere (Dennis et al., 2012). Although the CESM framework allows use of
229 grids with different resolutions for the atmosphere and land components depending on the
230 scientific purpose, here, identical grids are used which allow better simulation of terrain-
231 associated climatic features.

232 For our control simulation, we use the quasi-uniform 1° spectral element grid which is
233 obtained by dividing each cube face into 30×30 spectral elements. Hereafter, this grid is denoted
234 as ne30, referring to the number of elements along the edge of a cubed-sphere face. We employ
235 two VR grids. The grid with the highest resolution of 0.25° (~ 28 km) over the study domain
236 (Figure 1a) has a 1° base resolution and a transition zone of 0.5° in between the high and coarse
237 resolutions. This set up takes into account the spatial spin up of transiting flows (Matte et al.,

238 2017) which is necessary for the development of small scale features from the low-resolution
 239 driving lateral boundary conditions as permitted by the finer resolution. The other grid with the
 240 highest resolution of 0.125° (Figure 1b) also has the same 1° base resolution, but includes two
 241 transition zones of 0.5° and 0.25° . These two VR grids are labeled as ne30x4 and ne30x8,
 242 respectively, following the same nomenclature as above. The highest resolution domains of the
 243 VR grids have an approximate latitudinal extent of 23° - 59° N and longitudinal extent of 10° W-
 244 56.5° E. These three grids consist of 5400, 10212, and 20688 spectral elements, respectively. As
 245 a reference, a 0.125° quasi-uniform spectral element grid would consist of 86400 spectral
 246 elements – more than a factor of 4 as large as our finest VR grid. Throughout this study, the
 247 analysis domain is defined as the interior-most area with the highest resolution of VR grids.
 248

249

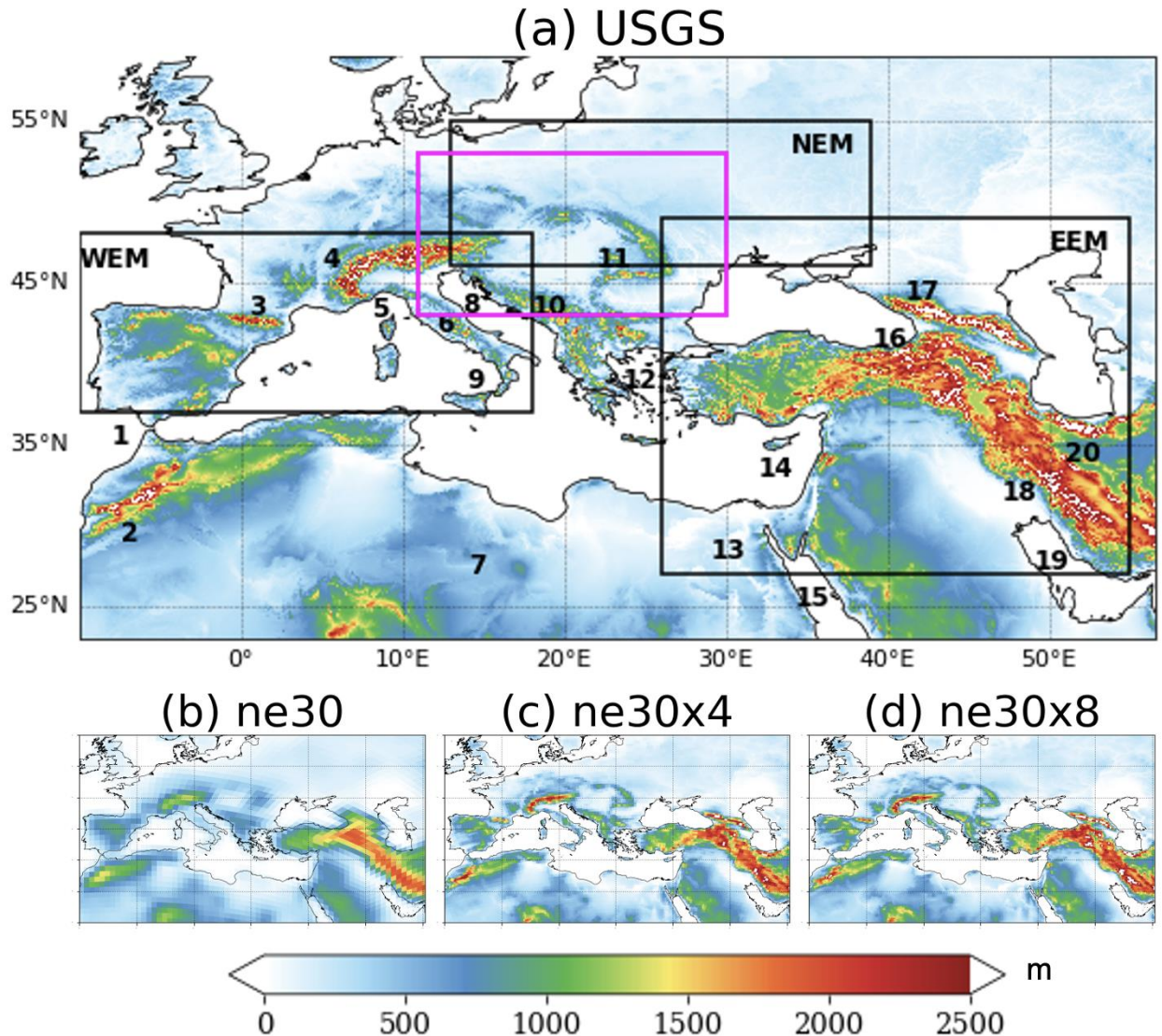


250

251 **Figure 1.** Variable resolution cubed-sphere grids. (a) Grid which has 1° base resolution with the
 252 highest resolution of 0.25° over the Euro-Mediterranean region (ne30x4). (b) As in (a) but with
 253 the highest resolution of 0.125° over the domain (ne30x8). Notice how the grid transition is done
 254 gradually.

255 2.1.2 Domain of Interest and Topographical Representation

256 The notable geographical features of the study domain are provided in Figure 2a, which
 257 depicts the real topography of the region at a resolution of 30 arc-seconds (~ 1 km) from the US
 258 Geological Survey (USGS; Danielson & Gesch, 2011) dataset – which was updated to include
 259 more accurate elevations of Greenland and Antarctica (Wijngaard et al., 2023) – using NSF
 260 NCAR's global model topography generation software package (Lauritzen et al., 2015). Figures
 261 2b, 2c, and 2d show the representation of this topography in the three model resolutions.



262

263 **Figure 2.** Representation of land topography in (a) the USGS dataset, (b) ne30, (c) ne30x4, and
 264 (d) ne30x8 grids. Model topographies are plotted on their respective native grids. The map in (a)
 265 also shows the most relevant geographical features of the Euro-Mediterranean region. The
 266 numbers denote the following features of the region: 1. Strait of Gibraltar; 2. Atlas Mountains; 3.
 267 Pyrenees; 4. European Alps; 5. Gulf of Genoa; 6. Apennines; 7. Sahara Desert; 8. Adriatic Sea;
 268 9. Tyrrhenian Sea; 10. Dinaric Alps; 11. Carpathians; 12. Aegean Sea; 13. Nile River; 14.
 269 Levantine Basin; 15. Red Sea; 16. Kackar Mountains; 17. Caucasus Mountains; 18. Zagros
 270 Mountains; 19. Persian Gulf; 20. Alborz Mountains. Subregions denoted with black boxes in (a)
 271 and abbreviations at their upper corners, and the one denoted with a magenta box are used for
 272 subregional analyses in this work. Here, WEM, NEM, and EEM denote western, northern, and
 273 eastern Euro-Mediterranean, respectively.

274 Quasi-uniform 1° resolution uses a rather smooth topography (Figure 2b) to maintain
 275 numerical stability and prevent numerical artifacts, a requirement at relatively coarse resolutions
 276 (Zarzycki et al., 2015). As such, it can neither resolve the rapidly varying features nor faithfully
 277 represent the topographic details such as mountain peaks of the Euro-Mediterranean region.

278 Impacts of smoothing are particularly evident in the representation of maximum elevation areas.
 279 In ne30x4, the 0.25° resolution substantially improves the representation of the details of the
 280 regional topography with many topographic features and their elevations closely matching those
 281 of the USGS dataset (Figure 2c). Increasing the regional resolution further to 0.125° in ne30x8
 282 does not seem leading to obvious additional improvements (Figure 2d) and it is quite similar to
 283 that of 0.25°.

284 2.1.3 Experimental Setup

285 Four sets of simulations were performed for this study as summarized in Table 1. The
 286 first set uses the quasi-uniform 1° grid where each element is divided in 3x3 (pg3) quasi-uniform
 287 resolution physics columns (Herrington et al., 2019) and it is referred to as ne30-n with “n”
 288 indicating that no parameter tuning is applied to the default ones in the base code. The second set
 289 of simulations uses the ne30x4 grid, again with no parameter tunings. This set is labeled as
 290 ne30x4-n. The third set, ne30x4-t, uses the ne30x4 grid, but some parameters are tuned as
 291 discussed below. The fourth set employs our highest resolution grid with the same tunings as in
 292 the ne30x4-t simulations. This set is referred to as ne30x8-t. The physics timesteps are reduced
 293 with finer resolutions which proportionally determines the other timesteps used. Throughout the
 294 manuscript “coarsest / finest (highest-resolution) simulation” will be used interchangeably with
 295 “ne30-n / ne30x8-t”.

296 **Table 1**
 297 *Model Simulations*

Configuration name	Grid resolution	Ensemble size	Physics timesteps (s)	Number of cores/ Simulation cost*	Modifications from the base code
ne30-n	Quasi-uniform 1°	7	1800	1800 / 2,306	-
ne30x4-n	1°→ 0.25°	7	450	3600 / 14,224	-
ne30x4-t	1°→ 0.25°	7	450	3600 / 14,224	Tuning
ne30x8-t	1°→ 0.125°	1	225	4320 / 48,689	Tuning – updated topography source data

298 *Note.* *Simulation cost is given in core-hours per simulation year.

299 All the simulations are performed for the 1998-2014 period. The first 2 years of data are
 300 discarded as spin-up. Thus, we analyze monthly and daily output fields for the 2000-2014 period,
 301 a length deemed long enough to provide a representative climate of the region, including its
 302 internal variability. We ran 7 ensemble members for ne30-n, ne30x4-n, and ne30x4-t where the
 303 ensemble spread is achieved by round-off level perturbations of the atmospheric potential
 304 temperature field at initialization. However, due to its high computational cost, we ran just one
 305 member for ne30x8-t.

306 2.1.4 Parameter Tuning

307 Default CAM physics parametrizations are developed for use in coarse resolutions of
 308 order 1°. Because the default parametrizations in CESM / CAM might not be appropriate for
 309 higher resolutions with lower time steps as we use in our study, some time-stepping errors are

310 likely to be seen. Thus, we might expect better simulation of the climate by properly tuning
 311 related parametrizations.

312 Climate models involve many parameters which are tunable, that is, which are not
 313 strongly constrained by process-level observations or theory (Schmidt et al., 2017) and are
 314 subject to uncertainty. In this study, we modify four radiative tuning parameters (see below)
 315 targeting those which largely impact energy budget through their effects on the simulation of
 316 radiation, and compare the results with the non-tuned version of VR-CESM. Increasing the
 317 horizontal resolution is likely to cause deficiencies in the representation of clouds via effects on
 318 the resolved-scale boundary layer properties (Xie, S. et al., 2018). Indeed, regional top of
 319 atmosphere (TOA) longwave and shortwave cloud forcing biases worsen in 0.25° simulations
 320 compared to those with 1° (e.g., from ne30-n to ne30x4-n) (see Figures 14 and 15). The
 321 shortwave cloud forcing (SWCF) is the net solar flux (FSNT) minus the clearsky net solar flux
 322 (FSNTC) at top of the model. Similarly, the longwave cloud forcing (LWCF) is the clearsky net
 323 longwave flux (FLNTC) minus net longwave flux (FLNT) at top of the model. When positive
 324 (negative), SWCF and LWCF indicate that the clouds have a warming (cooling) effect.
 325 Specifically, low-level clouds (e.g., shallow cumulus and stratiform clouds) largely modulate
 326 SWCF by reflecting incoming solar radiation, and high-level clouds (e.g., cirrus clouds)
 327 modulate LWCF by influencing the amount of outgoing longwave radiation. Therefore, low/high
 328 clouds have a negative/positive effect on the Earth's radiative balance. By modifying those
 329 tunable parameters, we target a better agreement with observations for LWCF and SWCF,
 330 addressing the degradation caused by increasing resolution.

331 **Table 2**
 332 *Physics Parameterization Modifications in the Tuned Simulations*

Parameter	Description	Component / Scheme	Non-Tuned value	Tuned value
clubb_c11b	High skewness of buoyancy damping for the third moment of vertical velocity	CAM / CLUBB microphysics	0.35	0.375
micro_mg_dcs	Auto-conversion size threshold from cloud ice to snow	CAM / MG2 microphysics	500×10^{-6} m	1000×10^{-6} m
r_snw	Base snow grain radius	CICE / Delta-Eddington	1.25 standard deviations	1.50 standard deviations
dt_mlt	Snow melt onset temperature	CICE / Delta-Eddington	1.5°C	1.0°C

333 Among several tunable parameters, we choose the ones listed in Table 2, following
 334 Wijngaard et al. (2023) as the parameters which have a major influence on the cloud formation.
 335 First, to increase low-level cloudiness, we increased the damping on vertical velocity skewness
 336 in CLUBB (clubb_c11b). clubb_c11b is one of the most impactful parameters for shallow
 337 convection and thus for the formation of low clouds (Guo et al., 2015). Increasing its value
 338 favors LWCF by damping buoyancy velocities, which reduces the vertical skewness of cloud
 339 distribution and consequently increases the fraction of low clouds.

340 Second, to thicken high clouds, microphysical auto-conversion size threshold for ice to
 341 snow (micro_mg_dcs) was increased. micro_mg_dcs is a MG2 microphysics parameter
 342 specifying the threshold for a cloud ice particle must grow before it is converted to snow. Larger
 343 values of this parameter mean retention of larger ice particles within glaciated clouds. This
 344 reasonably leads to larger LWCF because the duration before cloud particles precipitate
 345 increases.

346 Finally, for the purpose of cooling the high latitudes, shortwave radiation and albedo over
 347 sea-ice and snow increased by increasing base snow grain radius (r_{snw}) and decreasing snow
 348 melt onset temperature (dt_{mlt}) in the sea ice component. These adjustments of the optical
 349 properties of snow and sea ice change the base albedos and consequently influence shortwave
 350 radiation absorbed by Earth's surface (Briegleb & Light, 2007).

351 With these tunings, we obtain a new 7-member ensemble (ne30x4-t). The single ne30x8-t
 352 simulation was also run with the same tunings.

353 2.2 Evaluation Methodology

354 To evaluate our simulations, various observational, reanalysis, and satellite-derived
 355 datasets are used as summarized in Table 3. These datasets are generally preferred for their
 356 relatively high spatial and temporal resolutions.

357 **Table 3**
 358 *Summary of the Datasets Used in This Study*

Dataset	Spatial / Temporal resolution	Field used in the analysis	Source and reference
CRU TS v. 4.05	0.5°x0.5° (All land areas (excluding Antarctica) / Monthly	2m Temperature (T2m), Precipitation	Climatic Research Unit (Harris et al., 2014; Harris et al., 2020)
CPC	0.5°x0.5° / Daily	Daily max temperature and precipitation rate	NOAA Climate Prediction Center (Chen et al., 2008; Xie, P. et al., 2007)
E-OBS v. 27.0e	0.25°x0.25° / Daily	Daily precipitation rate	European Climate Assessment & Dataset initiative (Cornes et al., 2018)
ERA5	0.25° x 0.25° (37 pressure levels) / Monthly	Horizontal winds, vertical wind velocity, relative humidity, specific humidity, snow depth	European Centre for Medium-Range Weather Forecasts (ECMWF) (Hersbach et al., 2020)
CERES EBAF v.4.2	1°x1° / Monthly	Shortwave and longwave cloud radiative forcing (SWCF and LWCF)	NASA (Kato et al., 2018; Loeb et al., 2017)
AMSR2	0.25° x 0.25° / Monthly	Column integrated water vapor	Japan Aerospace Exploration Agency (JAXA) (Wentz et al., 2014)

359
 360 We evaluate the climatological performance of simulations with respect to T2m and
 361 precipitation using Climatic Research Unit gridded Time Series (CRU TS v.4.05) monthly data.
 362 CRU TS dataset is constructed by interpolation of monthly climate anomalies from
 363 meteorological stations across the land areas excluding Antarctica. For daily maximum T2m,
 364 NOAA Climate Prediction Center (CPC) dataset is utilized. CPC daily data and the European
 365 Climate Assessment & Dataset initiative (E-OBS) data are used for daily precipitation rate. E-
 366 OBS data cover Europe and Northern Africa. The fifth generation European Center for Medium-
 367 range Weather Forecast (ECMWF) atmospheric reanalysis (ERA5) data at single and pressure
 368 levels, combining past observations with models using data assimilation techniques, are used for
 369 performance analysis of fields such as horizontal and vertical winds, relative humidity, specific
 370 humidity, and snow depth and for quantities calculated by using these fields such as the
 371 vertically-integrated vapor transport (IVT). The Clouds and the Earth's Radiant Energy System
 372 (CERES) Energy Balanced and Filled (EBAF) dataset is used to evaluate shortwave and
 373 longwave cloud forcings. The Advanced Microwave Scanning Radiometer 2 (AMSR2)
 374 microwave satellite data are used in comparisons for column integrated water vapor.

375 We use root-mean-square-error (RMSE), which is the root of the mean of the squared
376 errors between the simulated and observed values, and relative root-mean-square-error (rRMSE),
377 which quantifies the model performance relative to observations as percentages to evaluate our
378 simulations. While RMSE has the same unit as the field being evaluated, rRMSE is a
379 dimensionless measure. In the evaluation of the total precipitation rate, grid points receiving less
380 than 1 mm/d annual precipitation are excluded from the calculations of rRMSE to avoid
381 exaggeration of biases and to better interpret the influence of increased resolution. Scale-
382 dependent skill of the simulations is quantified via pattern correlation coefficients between the
383 simulations and observations. Significance of differences between simulated and observed values
384 is assessed employing a two-tailed Student's t-test with a p-value of 0.05. Given that the model
385 output data both on land and ocean, whereas, the observational dataset, CRU, provides data over
386 land only, to compare the areal means of T2m and precipitation from the simulations with that
387 of observation over land, model data are masked based on Natural Earth's land shapefile at
388 1:10m scale (<https://www.naturalearthdata.com/>, (accessed on 9 October 2023)).

389 To enable direct comparisons of simulated fields with those of the above observational
390 and reanalysis datasets, model output files were regridded onto the respective regular longitude-
391 latitude grids of the datasets. For this purpose, we employ a first-order conservative mapping
392 procedure from the Earth System Modeling Framework (ESMF) library. This is a method which
393 preserves the integral, i.e., conservation, of the source field across regridding and supports
394 regridding between unstructured and structured grids. Because CAM6 uses hybrid pressure
395 coordinates in the vertical, we also perform logarithmic vertical interpolation to the respective
396 level coordinates of the evaluation datasets when necessary.

397 For long-term climatological analysis, we use ensemble means of ne30-n, ne30x4-n, and
398 ne30x4-t simulations and the single member of ne30x8-t simulation. When analyzing climate
399 extremes for precipitation over sub-regions, we check whether this single member lies within the
400 ensemble spread of other simulations by using all members of the ensembles.

401 **3 Results and Discussion**

402 In this section, simulation results are compared with observations and reanalysis
403 products. Subsections 3.1 and 3.2 are devoted to precipitation and T2m, respectively. Subsection
404 3.3 documents the representation of extreme daily maximum temperature and precipitation.
405 Effects of parameter tuning are discussed in subsection 3.4.

406 **3.1 Precipitation**

407 Simulation of precipitation is challenging, largely because it depends on small-scale
408 processes that need to be parametrized. Parametrization leads to uncertainties such as those
409 related to the cloud processes. For regions with high spatial heterogeneity, like our study domain,
410 interactions with the surface features (e.g., orography, coastlines, and land-sea contrasts) add
411 much more complexity (Flato et al., 2013). This difficulty is present for the interpretation of
412 results as well. Because so many scales are interacting with each other, sources of errors should
413 be understood well to avoid misinterpretations (Di Luca et al., 2021).

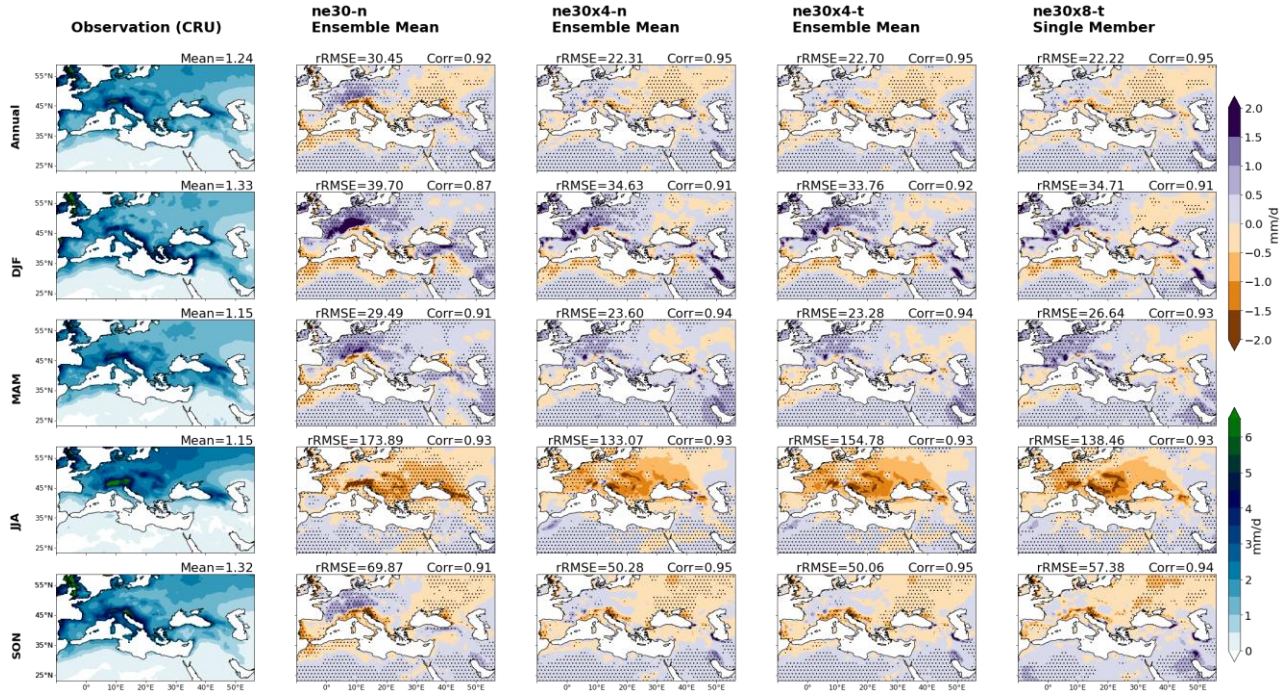
414 For precipitation, unless the resolution is increased to more than that of deep-convection-
415 permitting scales (i.e., < 4 km) in order to mostly eliminate the parameter dependency, added
416 value of increased resolution is limited to certain regions such as those with sharp topographic
417 contrasts (e.g., near high elevation terrain and coastlines). The effect of higher spatial resolution

418 is not expected to be seen distinctively for processes occurring at scales that can already be
419 resolved by coarser resolutions over homogenous terrain. Moreover, increasing resolution many
420 times leads to increased biases because the model parameterizations are often tuned for coarse,
421 operational resolutions as discussed above.

422 With these caveats, overall, all simulations produce the spatial variability of regional total
423 precipitation in good agreement with observations with relatively high pattern correlations
424 between 0.87-0.95 (Figure 3 and Figure S1). We see high precipitation in the northwest of the
425 study domain, particularly over windward sides of mountain ridges, and at the west coasts, and
426 low precipitation in the south (Northern Africa and Arabian Peninsula). The correlations for VR
427 simulations are typically higher than that of the coarse control simulation.

428 For quasi-uniform 1° control simulation, the largest/smallest biases are seen in JJA/MAM
429 (rRMSE values for ne30-n are 39.7, 29.5, 173.9, and 69.9% for DJF, MAM, JJA, and SON,
430 respectively) (Figure 3). The amplitudes of wet/dry biases over the windward/leeward sides of
431 the high mountains and the dry biases over the coasts exceed 2 mm/d in some seasons and
432 regions (e.g., wet/dry bias on the windward/leeward side of European Alps in DJF/MAM and dry
433 bias in the east coast of Black Sea in JJA). Increasing resolution from 1° to 0.25° (compare the
434 columns corresponding to ne30-n and ne30x4-n simulations, respectively) improves the model
435 performance annually and seasonally (rRMSE values for ne30x4-n are 34.6, 23.6, 133.1, and
436 50.3% for DJF, MAM, JJA, and SON, respectively). The wet/dry biases over the
437 windward/leeward sides of the high mountains and dry biases at the western coasts substantially
438 reduce with increased resolution. Parameter tuning (i.e., from ne30x4-n to ne30x4-t) degrades
439 model performance for JJA, largely because of the expansion of the higher magnitude dry biased
440 area over the eastern Europe, whereas it leads to improvements in other seasons (rRMSE values
441 for ne30x4-t are 33.8, 23.3, 154.8, and 50.1% for DJF, MAM, JJA, and SON, respectively).
442 Further increasing the resolution (i.e., from ne30x4-t to ne30x8-t) overcomes this degradation in
443 JJA to some extent but leads to slightly larger biases than that of ne30x4-t in other seasons
444 (rRMSE values for ne30x8-t are 34.7, 26.6, 138.5, and 57.4% for DJF, MAM, JJA, and SON,
445 respectively). The improvement in JJA shows that, the highest resolution simulation (ne30x8-t)
446 is able to resolve more smaller scale processes related to convective activity which dominates
447 summer precipitation and it leads to an apparent improvement despite the degradation (as seen in
448 other seasons) related to lack of extra parameter tunings.

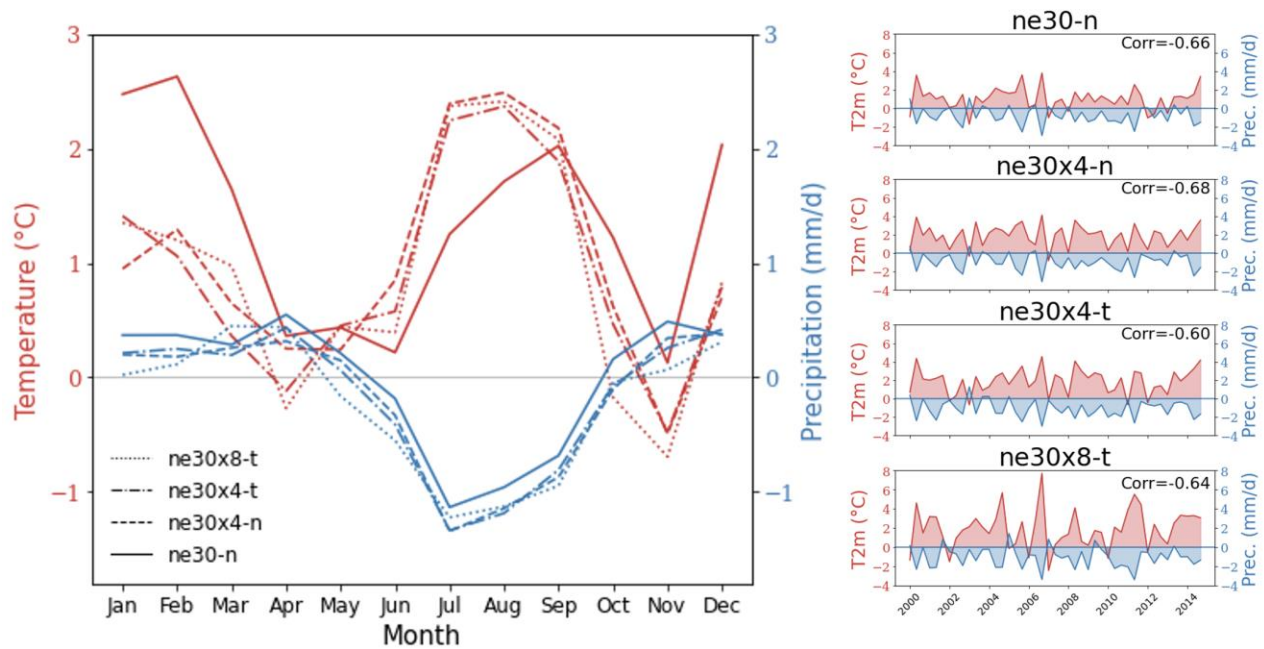
449 The precipitation bias contrast on the windward/leeward sides of high mountains, which
450 can exceed ~ 7 mm/d in places for ne30-n, is reduced with increased resolution as a
451 demonstration of added value of VR-CESM. It is a manifestation of improved orography which
452 better resolves adjacent topographical gradients (i.e., sharp topographical contrasts) leading to
453 better simulation of moisture convergence. Another added value of increased resolution is seen
454 on the coastlines. The biases seen for ne30-n over the western coasts (e.g., dry biases over the
455 west coasts of Iberian Peninsula in MAM and SON; northwestern coast of Africa in DJF, MAM
456 and SON; southwest coast of Türkiye in DJF; and easternmost coast of the Mediterranean Sea in
457 DJF) diminishes with increased resolution. An explanation for these reductions in coastal biases
458 will be discussed later.



459

460 **Figure 3.** Observational annual- and seasonal-mean (rows) distributions (first column) and
 461 model (ne30-n, ne30x4-n, ne30x4-t, and ne30x8-t in order) minus observations annual and
 462 seasonal difference distributions for precipitation (other columns). The observations are from
 463 CRU. Relative root-mean-square-errors (rRMSE) and pattern correlations as well as the areal
 464 means for observations are given at the top of each panel. rRMSE is calculated for the grids with
 465 annual precipitation more than 1 mm/d. The dots indicate areas where the differences are
 466 statistically significant at the 95% level based on two-sided Student t-test. The observations and
 467 difference distributions use the lower and upper color bars, respectively.

468 Some persistent precipitation biases remain at all resolutions. For example, in summer, a
 469 warm and dry bias over the Central-Eastern Europe exists in all simulations (Figures 3 and 9). To
 470 investigate reasons for this persistent bias, we study the relationship between T2m and
 471 precipitation over the region shown in magenta in Figure 2a. We show the annual cycles of T2m
 472 and precipitation biases and their time series in Figure 4. For all simulations, there exists a
 473 statistically significant (with a p-value of 1.3×10^{-5} or smaller) strong anti-correlation (with an
 474 amplitude of 0.60 or more) between these two biases (Figure 4 – right) indicating a causal
 475 relationship between these two surface variables over this region. The peaks of the precipitation
 476 deficit occur almost at the same time (in July) for all resolutions. The temperature excess peaks
 477 in August/September for VRCEM/quasi-uniform 1° simulations respectively and precipitation
 478 deficit precedes the temperature excess in this respect (Figure 4 – left).



479

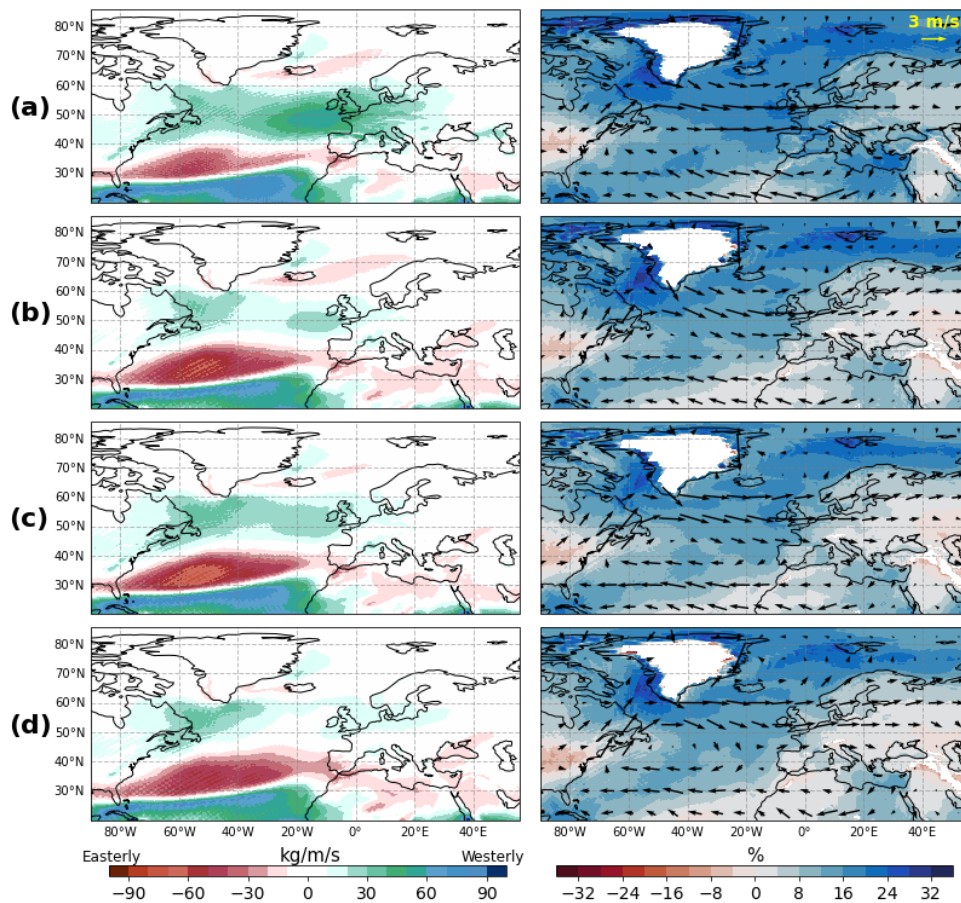
480 **Figure 4.** Anti-correlation between precipitation and T2m in summer for the analysis region
 481 shown with a magenta box in Figure 2a. Left: Annual cycles of temperature (red) and
 482 precipitation (blue) biases; right: Time series of biases of temperature (red) and precipitation
 483 (blue). In the time series plots, the correlation coefficients are provided at the upper right corner
 484 of each panel.

485 The warm bias over the region can be attributed to the land-atmosphere interactions
 486 following the precipitation deficit. The time lag between precipitation deficit and temperature
 487 excess is consistent with development of related mechanisms. The mechanism, as proposed by
 488 several studies (e.g., Lin et al. 2017; Vautard et al., 2007), should be working as follows:
 489 Precipitation deficit leads to soil moisture deficit which results in less evaporative cooling and
 490 ultimately higher temperatures. Underestimation of precipitation rates in simulations can be
 491 explained by less moisture transport due to the drier climate. As a further feedback, evaporative
 492 demand over land causes less cloud development and precipitation leading to further surface
 493 warming (Tuel & Eltahir, 2021).

494 A large wet bias is evident over the western Europe except in JJA with its highest
 495 magnitude occurring during winter months (DJF), when this region experiences its largest
 496 precipitation, and on the windward side of the European Alps. This bias largely diminishes with
 497 high resolution. Over the western Mediterranean land areas, the North Atlantic Ocean is the
 498 major moisture source especially in winter (Batibenz et al., 2020). Therefore, we investigate the
 499 mechanism behind this winter wet bias considering the large-scale dynamics of the atmospheric
 500 circulation. For this analysis, we employ ERA5 reanalysis data for evaluation of the model
 501 solutions because ERA5 provides all the needed fields, i.e., relative humidity and horizontal
 502 winds at pressure levels as well as the calculated IVT at relatively high horizontal and vertical
 503 resolutions ($0.25^{\circ} \times 0.25^{\circ}$ and 37 pressure levels, respectively).

504 We present model minus ERA5 difference distributions for IVT, 850-hPa wind vectors,
 505 and relative humidity for winter (DJF) in Figure 5. Both coarse and high-resolution simulations
 506 show positive IVT differences directed towards the western Europe at mid latitudes. IVT biases

507 exceed $60 \text{ kg m}^{-1} \text{ s}^{-1}$ for ne30-n and $20 \text{ kg m}^{-1} \text{ s}^{-1}$ for VR simulations (Figure 5 - left). It is clearly
 508 seen that 850 hPa westerly wind difference vectors carry North Atlantic moisture right over the
 509 wet-biased area in the Northwestern Europe in all simulations (Figure 5 - right). Strength and
 510 orientation of wind difference vectors and vapor transport are consistent with the magnitude of
 511 wet bias for different resolutions. Over the area with stronger moisture transport, relative
 512 humidity is also higher in the simulations. Overestimation of relative humidity reaches to more
 513 than 20% for ne30-n, 12% for ne30x4-n and ne30x4-t, and 8% for ne30x8-t. There is a notable
 514 reduction in relative humidity with increasing resolution which is also discussed in Herrington
 515 and Reed (2017). Therefore, the wet bias can be attributed to the larger precipitation produced by
 516 stronger wind difference vectors with a direction in favor of carrying moisture over the wet-
 517 biased area, together with higher relative humidity. The improvement in this bias with higher
 518 resolution is related to better representation of water vapor transport from the North Atlantic at
 519 these resolutions.
 520

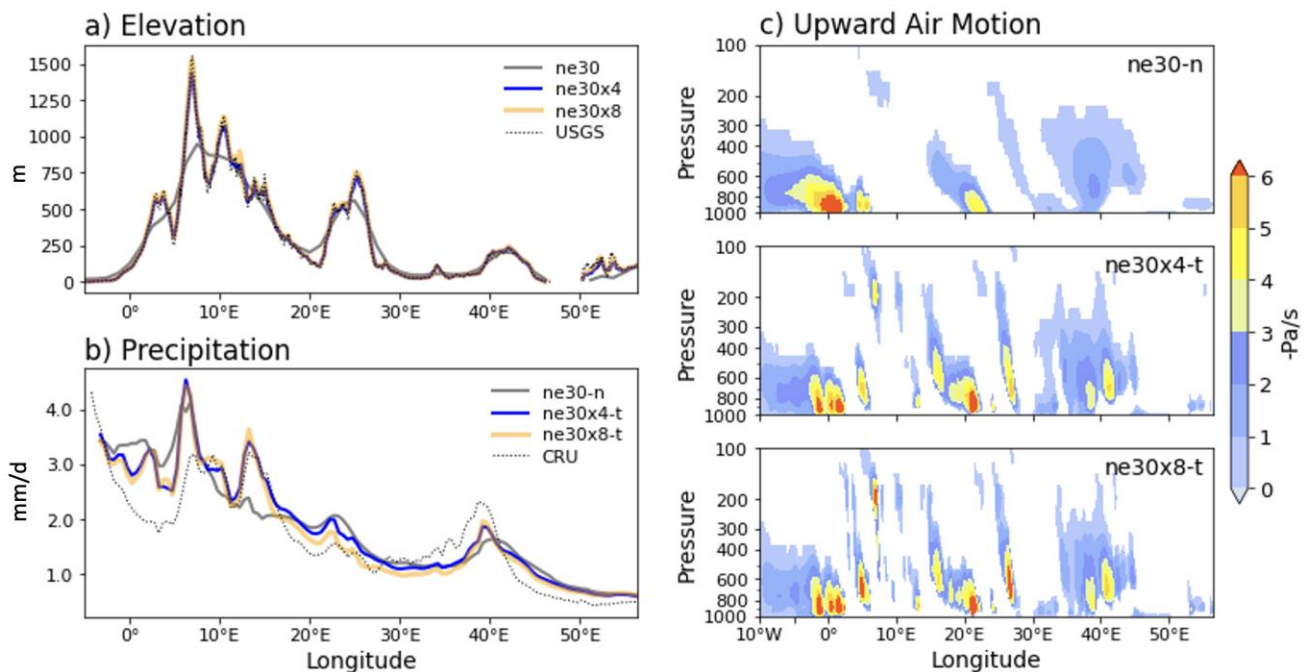


521
 522 **Figure 5.** Differences (simulations-ERA5) of vertically-integrated vapor transport (IVT) (left),
 523 and 850 hPa winds (vectors) and relative humidity (right) for DJF; a) ne30-n, b) ne30x4-n, c)
 524 ne30x4-t, and d) ne30x8-t.

525 The orientation and strength of the 850 hPa wind differences can be explained by
 526 geopotential height differences at 500 hPa, the level which is commonly used to investigate the
 527 large-scale circulation. Figure S2 shows the differences of 500 hPa geopotential height between
 528 VR simulations and the control simulation for DJF. There is a positive height difference between

529 the VR simulations and control simulation over the North Atlantic stretching into the North-
 530 Western Europe which is indicative of more cyclonic flow represented by the control simulation.
 531 Cyclonic activity orients moist air onto Western Europe. The negative sea level pressure bias
 532 over this region is also consistent with the higher intensity of low-pressure systems. This is a
 533 demonstration of the ability of VR-CESM in resolving dynamical processes driving precipitation
 534 along with its better topography treatment.

535 To highlight the role of orography in contributing to the precipitation rates in these
 536 simulations, we evaluate longitudinal distributions of precipitation within the latitude band
 537 between 44°N and 48°N which includes the European Alps. Figure 6 shows the elevation,
 538 precipitation, and vertical pressure velocity averaged along this latitude band for DJF – chosen
 539 for being the season when the advection of moisture from the North Atlantic is most prominent.
 540 Elevation is plotted for the three different grids (ne30, ne30x4, and ne30x8) used in the
 541 simulations and for the USGS dataset.



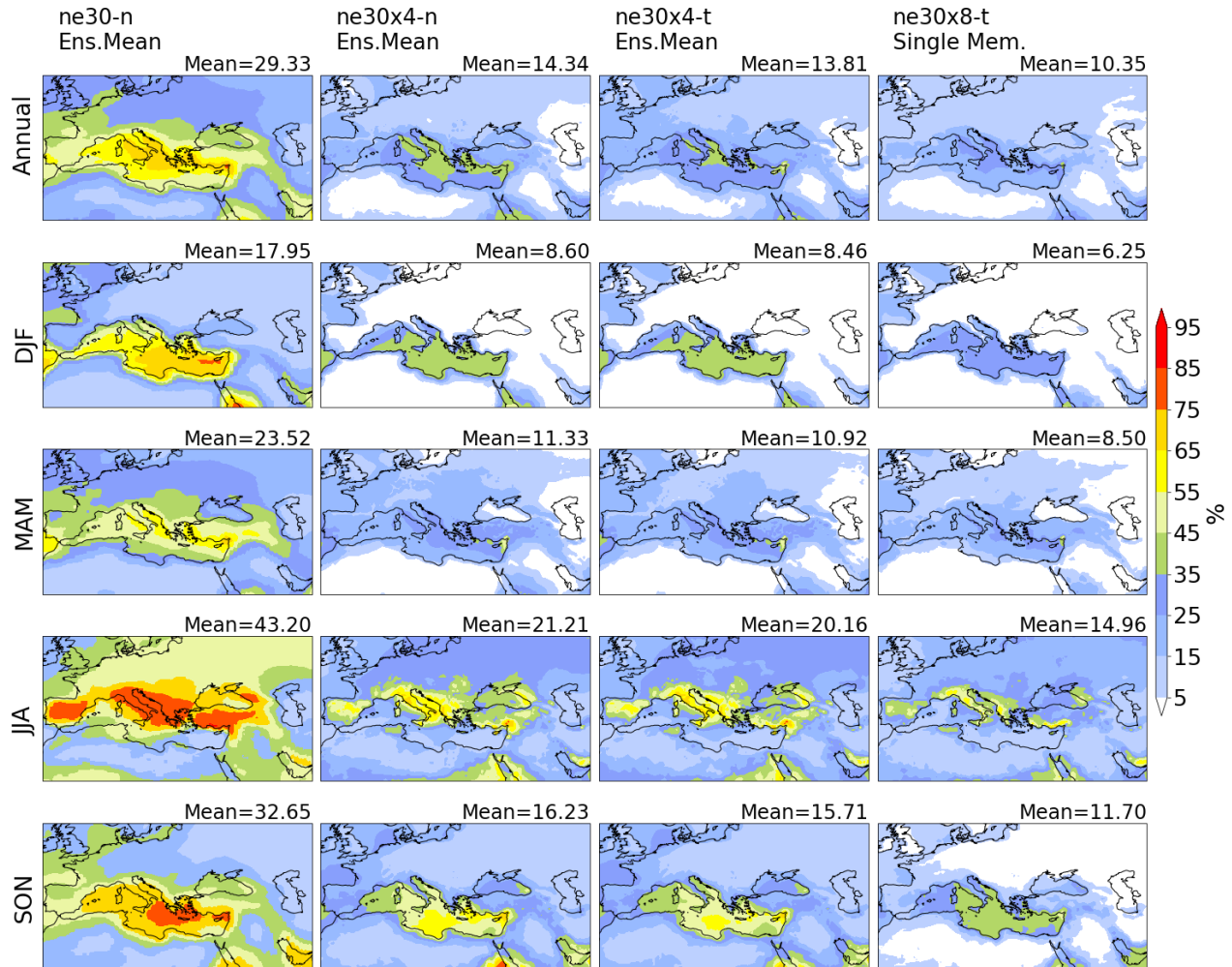
542

543 **Figure 6.** Longitudinal distribution of (a) terrain height, winter (b) precipitation rate and (c)
 544 vertical pressure velocity corresponding to upward motions (scaled with a factor of 100 and
 545 multiplied by -1) averaged over the latitude range of 44°- 48°N.

546 In simulations, the persistent wet bias over the northwest of the study domain during
 547 winter is clearly present across the windward side of the European Alps (~ 3°W-7°E). This wet
 548 bias is highest for ne30-n (up to more than ~1.5 mm/d). All simulations reach a maximum in
 549 precipitation at ~7°E at about 4.5 mm/d which then rapidly declines to the east. For ne30-n, this
 550 maximum precipitation rate is smaller than that of the VR simulations due to its smoother
 551 topography. The simulated maximum occurs a bit to the west compared to observations as a
 552 result of differences in the representation of elevation. ne30-n underestimates precipitation at the
 553 lee side (~ 8°-16°E). We see the typical dry bias over the Eastern Europe (~ 34°E-41°E and ~
 554 30°E-41°E for control and VR simulations respectively) which reaches ~0.6 mm/d (see also
 555 Figure 3). The precipitation rates for ne30x4 and ne30x8 are quite similar as a reflection of their

556 similar topographical representations. As shown in Figure 6c, the locations and expansions of
557 upward air motions represented by vertical pressure velocities better coincide with the respective
558 terrain upslopes and downslopes in VR-CESM high-resolution simulations. Orographically
559 forced upward motions are strongest and most vertically expanded for ne30x8-t.

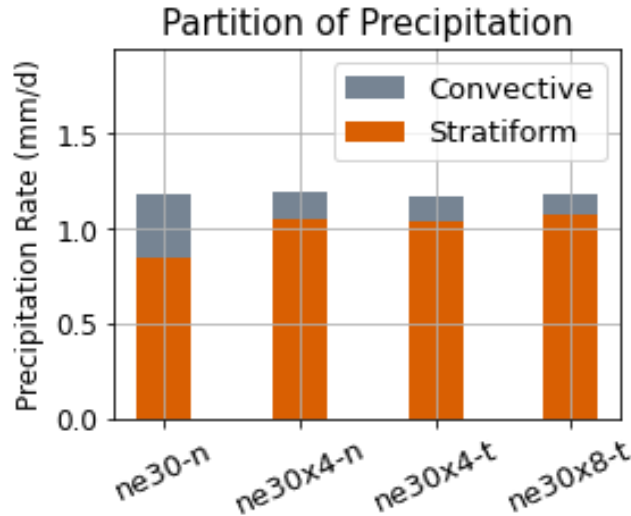
560 Reasonably, increased resolution might be expected to better resolve the convective
561 precipitation due to its ability to represent smaller scales at which convection takes place.
562 However, it is not the case for our simulations. Figure 7 shows the distribution of the fraction of
563 convective precipitation (i.e., the percentage of total precipitation contributed by convective
564 precipitation) for the simulations, annually and seasonally. In the region, maximum and
565 minimum convective precipitation fraction are seen in JJA and DJF, respectively, in all
566 simulations. It appears that while convective precipitation fraction decreases, large-scale
567 precipitation fraction increases with increased resolution. The coarsest and finest resolution
568 simulations produce the highest and lowest fraction of convective precipitation, respectively, in
569 all seasons. For instance, JJA fractions are 43.2 and 15.0% and DJF fractions are 18.0 and 6.3%,
570 respectively. In summertime, for the coarsest resolution, fraction of convective precipitation is
571 very high (more than 75%) over most of the southern Europe, Anatolia, and east coast of the
572 Black Sea, and it exceeds 45% over the rest of Europe and southwest Russia, Arabian Peninsula,
573 and northwest of Africa. For the highest resolution, relatively higher fractions (35-65%) are
574 confined to the coastal regions. The highest fractions are located over land in summer and they
575 shift to over sea as the seasons progress.



576

577 **Figure 7.** Annual- and seasonal-mean distributions of the fraction of convective precipitation.
 578 Areal means (as percentages) are given at the upper right of each panel.

579 The shift in the partitioning of convective and stratiform precipitation is a known
 580 phenomenon for CAM and for other atmospheric models as well. Consistently, in our
 581 simulations, the ratio of annual large-scale (stratiform) to total precipitation rate is lowest/highest
 582 and the ratio of convective to total precipitation rate is highest/lowest for the coarsest/finest
 583 simulation (Figure 8). This shift can be explained by the sensitivity of parametrized convective
 584 and stratiform precipitation rates to resolution following the causality set forth by Herrington and
 585 Reed (2020). In effect, the larger resolved upward vertical velocities supported at higher
 586 resolutions increasingly compete with the convection scheme to stabilize the atmosphere. These
 587 larger velocities facilitate subsidence as a consequence of mass conservation, which tends to dry
 588 out and stabilize the atmosphere further. The reduction in physics time-step also contributes to
 589 the reduction in convection scheme activity (Williamson, 2013).



590

591 **Figure 8.** Partitioning of stratiform and convective precipitations in simulations.

592 As an indicator of this progressive drying of atmosphere with increasing resolution, area
 593 weighted regional averages of simulated total (vertically integrated) precipitable water decreases
 594 with increasing resolution in our model results (15.69, 15.09, 15.26, and 15.06 kg/m²
 595 respectively for 1°, 1/4° (non-tuned and tuned), and 1/8°). Figure S3 shows differences of high-
 596 resolution simulations (ne30x4-n, ne30x4-t and ne30x8-t) from ne30-n for total precipitable
 597 water (TMQ). We note that ne30x8-t has the highest magnitude of differences and the negative
 598 differences follow the topography (e.g., the biggest and the smallest negative differences exist
 599 over the highest and the lowest elevations, respectively).

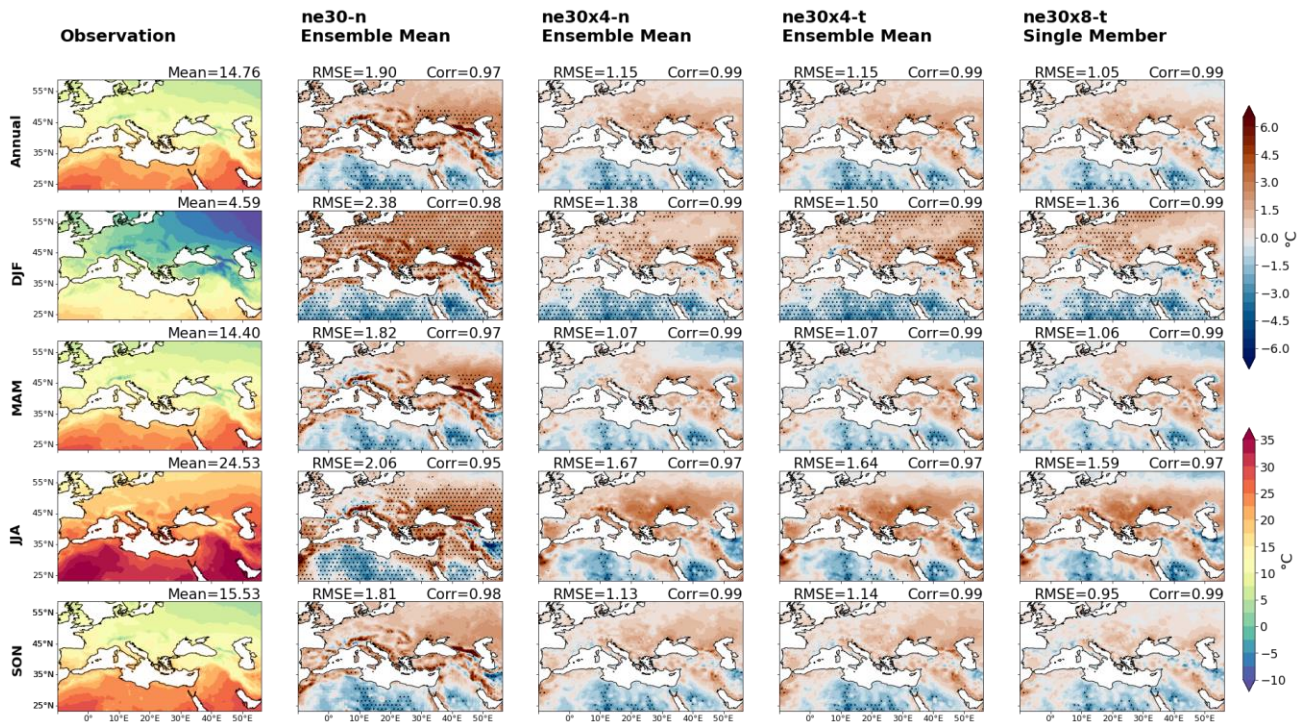
600 3.2 2-Meter Temperature (T2m)

601 Overall, all simulations are able to represent the spatial variability of T2m well with
 602 pattern correlations between 0.95-0.99 over the refined domain in all seasons (Figure 9 and
 603 Figure S4). The lowest (but still quite high) pattern correlations are seen in JJA. VR simulations
 604 have slightly higher correlations relative to ne30-n in all seasons. From a qualitative standpoint,
 605 existence of similar distribution patterns with quasi-uniform coarse resolution shows that
 606 variable resolution simulations produce credible climatic representations in terms of temperature.

607 Based on the regional averages, the coarsest and the finest resolutions tend to
 608 overestimate and underestimate, respectively, average T2m compared to observations both
 609 annually and seasonally (except a slight overestimation by the finest resolution in JJA). For
 610 example, the winter-mean T2m is 4.59, 5.22, and 4.35°C in CRU, ne30-n, and ne30x8-t,
 611 respectively, with the largest relative gap seen in winter (Figure S4). This finding can be partly
 612 attributed to the overestimation of T2m over mountainous regions in ne30-n due to its smooth
 613 topography and smaller overestimation or underestimation of T2m in ne30x8-t. It should be
 614 noted, however, that warm bias of CRU as a consequence of the scarcity of stations over
 615 mountainous regions can artificially contribute to the cold bias of high-resolution simulations
 616 (Giorgi et al., 2004). Also, a supporting explanation might be related to simulated and observed
 617 snow-ice albedo feedbacks. Because less snow leads to increased temperatures by absorbing
 618 more shortwave radiation, underestimation/overestimation of snow cover in ne30-n/ne30x8-t

619 (Figure S5) over high mountains might be contributing to higher/lower temperatures. As an
 620 indicator of less accurate representation of topographical heights, ne30-n shows a dry snow water
 621 equivalent bias at high elevations. For VR simulations, the snow bias over mountains, which
 622 worsens with elevation, could also be a result of incorrect lapse rates, because CESM has not
 623 been developed for small grid spacings such as ours (Rhoades et al., 2018).

624 There are statistically significant warm biases well exceeding 6°C over the mountains and
 625 coasts in ne30-n (Figure 9). Also, statistically significant cold biases over the southern regions
 626 exceed 5°C locally. For this coarsest simulation, DJF is the season showing the largest biases
 627 (with an RMSE of 2.4°C) and JJA is the season with the lowest pattern correlation value of 0.95.
 628 The impact of increased resolution in the representation of T2m is clearly seen in all seasons, as
 629 quantified by the RMSE values and also with a decrease in the total area with statistically
 630 significant differences from observations. For example, ne30x4-n has considerably lower RMSE
 631 values than ne30-n with higher pattern correlations (RMSE values of 1.4, 1.1, 1.7, and 1.1°C and
 632 pattern correlations of 0.99, 0.99, 0.97, and 0.99 for DJF, MAM, JJA, and SON, respectively).
 633 For ne30x4-n, JJA is the season with the largest biases and with the lowest relative improvement
 634 over ne30-n among other seasons, though still representing a considerable improvement.
 635 Parameter tuning applied to ne30x4-n yields mixed results. ne30x4-n and ne30x4-t simulations
 636 have quite similar bias patterns and equal pattern correlations in all seasons. A notable difference
 637 is seen in DJF, when RMSE value increases after tuning (from 1.38 to 1.50°C). ne30x8-t has the
 638 lowest biases in all seasons although further increasing the resolution does not result in a
 639 proportional improvement (as much as that is seen when resolution is increased to 0.25°). In this
 640 highest resolution simulation, JJA remains as the season with the largest biases as in both 0.25°
 641 simulations.



642
 643 **Figure 9.** Same as Figure 3 but for 2-m temperature. RMSE values are given at the upper left of

644 difference plots. The observations and difference distributions use the lower and upper color
645 bars, respectively.

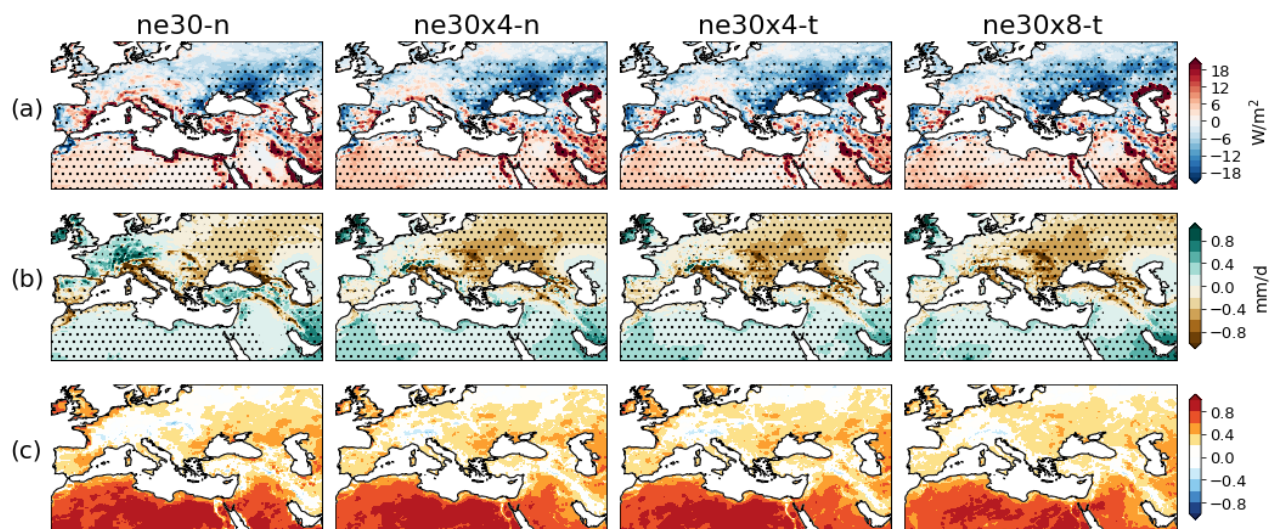
646 A general warm (cold) bias is seen over the northern (southern) parts of the region, which
647 persists in all seasons. Also, there exists a warm bias in Central-Eastern Europe which is most
648 pronounced in summer. These two persistent biases will be discussed later. Annually, most
649 prominent improvements are seen over high elevations such as the Atlas, Pyrenees, Alps,
650 Apennines, Caucasus, Kackar, Alborz, and Zagros mountains and at the coasts. The warm biases
651 over the high mountains and coasts decrease from more than 6°C to less than 2°C with increased
652 resolution. While overestimation of temperature at high elevation terrain, which typically occurs
653 throughout the entire year, is alleviated with higher resolution, the uncertainties of the
654 observational data, such as a possible bias towards low-elevation stations, cannot be ruled out.
655 Improvements are generally less pronounced in regions without strong orographic gradients
656 highlighting the added value of higher resolution resulting from having a better topographic
657 representation. For all configurations, typical warm biases over the west coasts and cold biases
658 over the southwest inlands can be partly attributed to the representation of extreme hot
659 temperatures in the simulations (Figure 11).

660 For analysis of the seasonal evolution of T2m, we divide the study domain as north and
661 south of 30°N following the Intergovernmental Panel on Climate Change's (IPCC) classification
662 of sub-regions (Iturbide et al., 2020). Over both subregions, all simulations capture the observed
663 seasonal cycle of T2m well (Figure S6). Both subregions show maximum temperature values in
664 summertime and minimum ones in wintertime while northern mean temperatures are consistently
665 ~10°C lower than the southern ones all over the seasonal cycle. For all simulations, we see a
666 small overestimation (less than ~1.5°C) during summer months (also during winter for ne30-n)
667 over the northern part and a small underestimation (less than ~2°C) throughout the year over the
668 southern part. These results are consistent with the spatial distribution of biases (Figure 9).

669 In VR simulations, summer stands out as the outlier with the highest magnitudes of
670 biases. It is the season when small scale processes dominate and topography has a prominent
671 influence. Therefore, we want to explore the ability of VR-CESM in representing the summer
672 circulation features over the Euro-Mediterranean region. During this period, the circulation over
673 the region is mainly dominated by an interplay of influences of the Azores High pressure system,
674 South Asian monsoon, a northerly flow (e.g., the Etesians), and the highly complex topography
675 of the region. A mechanism behind the subsidence causing hot and dry summers in the region is
676 suggested by Rodwell and Hoskins (1996) as a monsoon-desert mechanism. This mechanism is
677 also discussed in Simpson et al. (2015). Briefly, the subsidence in the region primarily exists due
678 to the remote diabatic heating of the Asian monsoon which induces a Rossby-wave pattern to the
679 west, extending into the Euro-Mediterranean region. The maxima and descent of the northerly
680 flow, which is synchronous with the monsoon convection, favors a stronger Rossby wave effect
681 by causing a weaker easterly jet (Tyrlis and Lelieveld, 2013). The Etesians are regional scale
682 low-level northerly winds blowing over the Aegean Sea Basin during the extended summer from
683 May to September (Dafka et al., 2016) with maximum persistence, intensity, and frequency
684 during July and August. The adiabatic warming occurring as a result of the large-scale
685 subsidence counteracted by the southward-blowing Etesian winds at the lower troposphere
686 inhibits cloud formation and convection causing dry summers with clear skies. Interaction of the
687 regional topography exerts a dominant influence in localizing the regions of the subsidence by
688 inducing orographically locked summer anticyclones and in amplifying the subsidence and the

689 northerly flow. As it is stated in Simpson et al. (2015), about 20% of the Mediterranean
 690 summertime moisture deficit can be attributed to the mountain-induced circulation. To
 691 understand the large-scale dynamics of the atmosphere, vertical wind velocity at the upper
 692 troposphere can be a useful field to look at. It shows the areas of upward motion/ascent and
 693 downward motion/subsidence. Our simulations are able to represent the summer subsidence-
 694 ascent pattern in agreement with the monsoon-desert mechanism mentioned above, also
 695 consistent with the ERA5 data (Figure S7). There is a subsidence over our study domain which is
 696 most pronounced over the Aegean Sea and an ascent over the South Asian monsoon region. The
 697 simulations are also able to capture the subsidence regions over the eastern Mediterranean and
 698 east of the Caspian Sea located at the eastern flanks of low-level (850 hPa) orographically locked
 699 anticyclones centered over the Northwest Africa and Zagros mountains. In summer, topography
 700 exerts the greatest influence on these subsidence patterns because it is the season when the low-
 701 level incident flow is easterly (which is westerly in other seasons).

702 Over the southern part of the study domain (Northern Africa and Arabian Peninsula), as
 703 noted earlier, there is a general cold bias in contrast to a general warm bias in the north. This
 704 southern cold bias can also be explained with land-atmosphere interactions. Figure 10 depicts the
 705 differences of the simulations from ERA5 for latent heat flux (Figure 10a) and precipitation
 706 (Figure 10b) as well as the correlations of latent heat flux and precipitation differences (Figure
 707 10c). Over the southern part, more precipitation (i.e. positive precipitation biases) drives more
 708 evapotranspiration. It leads to more evaporative cooling and results in a colder climate (Mueller
 709 and Seneviratne, 2014). Here, much higher proportion of the net radiation is transferred to the
 710 atmosphere by latent heat flux leading to positive latent heat flux biases (Figure 10a). Due to low
 711 rainfall rates this is a soil-moisture limited area. High positive correlations between the
 712 precipitation and latent heat differences indeed confirm the active soil moisture – latent heat flux
 713 coupling which is a characteristic of water limited regimes. Similarly, general warm biases over
 714 the north are also consistent with the underestimation of latent heat flux by all model
 715 simulations.



716

717 **Figure 10.** Annual differences of the simulations from ERA5 for (a) latent heat flux and (b)
 718 precipitation. (c) Correlations between precipitation and latent heat flux differences. Precipitation
 719 bias plots use ERA5 for consistency with the latent heat flux difference plots. The dots indicate

720 areas where the differences are statistically significant at the 95% level based on two-sided
721 Student t-test.

722 There are large positive biases of $> 20 \text{ W/m}^2$ for latent heat flux in ne30-n along the
723 coasts (e.g., the coasts of the Mediterranean Sea, the Red Sea, and the Persian Gulf). These
724 biases substantially diminish in higher resolutions. Song and Yu (2017) show that heat fluxes
725 better capture the complex air-sea interactions near the coastal areas in high-resolution
726 simulations where the coastlines and topography-related oceanic and atmospheric processes and
727 their complex interactions are better represented. In high-resolution simulations, there exist large
728 positive latent heat flux biases in the north of the Caspian Sea. This positive bias can be
729 explained by the differences between the land masks applied to these simulations and the ERA5
730 land-sea mask (Figure S8). Because the Caspian Sea is handled by the land component in CESM
731 in the ne30 runs (not by the ocean component as in the ne30x4 and ne30x8 runs) we do not see
732 that positive bias for ne30-n.

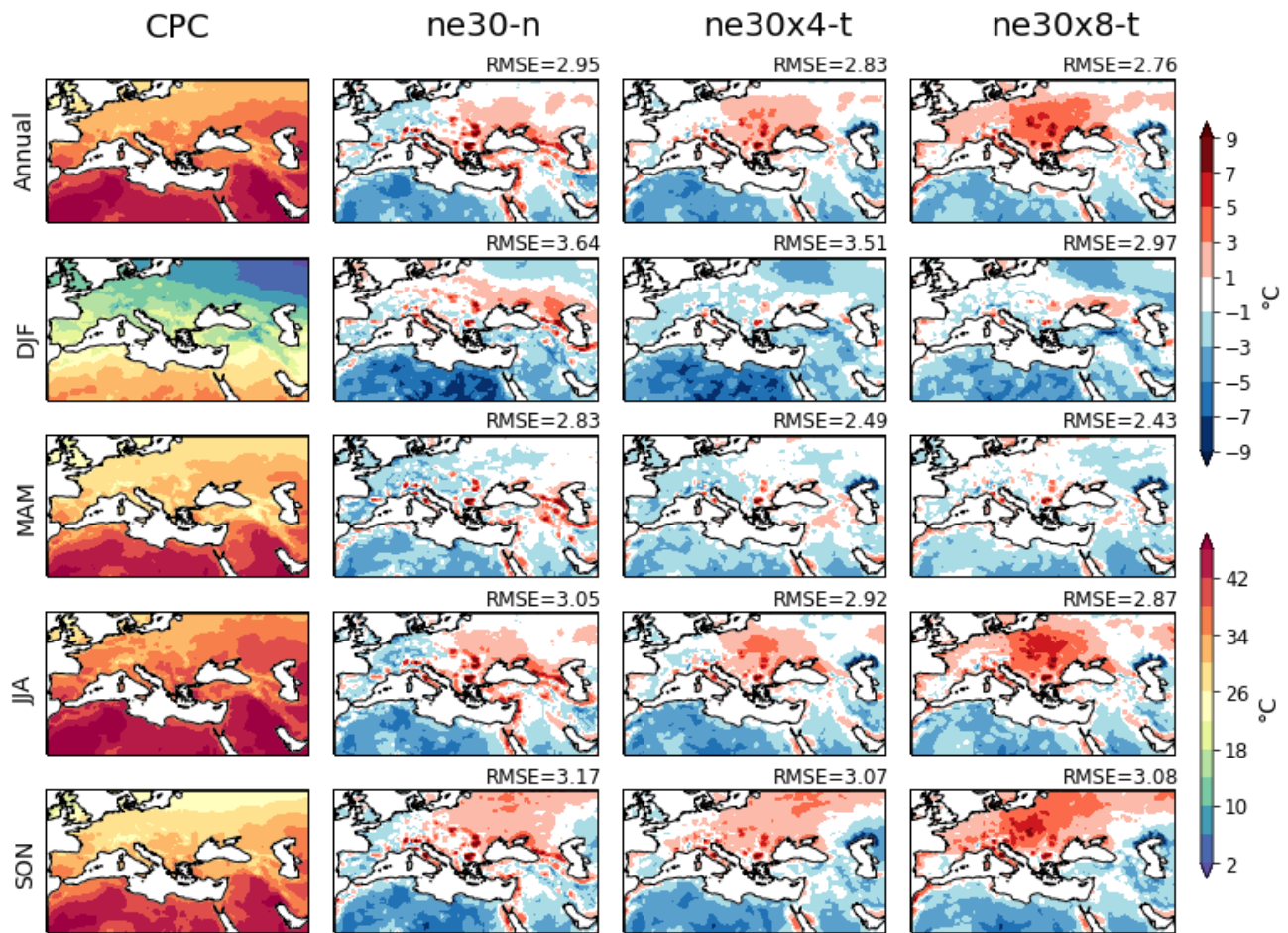
733 3.3 Climate Extremes

734 To evaluate how climate extremes are represented at different resolutions, we consider
735 the 99th percentile of daily precipitation and daily maximum T2m (Tmax). These are commonly
736 used metrics for defining climate extremes and they are also important for our region. For
737 observations, we use the CPC dataset for extreme daily temperatures and both E-OBS and CPC
738 datasets for daily extreme precipitation. Because we do not have daily outputs for ne30x4-n, it is
739 not included in this analysis.

740 3.3.1 Extreme Maximum Temperature

741 Figure 11 shows observational distributions of the 99th percentile of daily maximum
742 temperatures (first column) and differences of the simulations from observations (other
743 columns). The highest maximum temperature values occur over the south of the region (Northern
744 Africa and Arabian Peninsula) reaching more than 45°C whereas the lowest values are over the
745 northern and high elevation regions. In the south, although there are several overestimated
746 coastal areas, the simulations generally underestimate daily maximum temperatures. This
747 underestimation is likely contributing to the southern cold bias of monthly mean temperatures.
748 Similarly, the time-mean warm biases over the northern latitudes (Figure 9) are partly due to
749 overestimation of extreme hot temperatures. As an added value of high resolution, ne30x8-t
750 shows the smallest underestimation in the south in all seasons. For ne30-n, ne30x4-t, and
751 ne30x8-t, the respective seasonal biases are as follows: DJF: 3.64, 3.51, and 2.97°C ; MAM:
752 2.83, 2.49, and 2.43°C ; JJA: 3.05, 2.92, and 2.87°C ; and SON: 3.17, 3.07, and 3.08°C .
753 Increasing resolution from 1° to 0.25° (from ne30-n to ne30x4-t) decreases biases with the
754 greatest improvement occurring in MAM. Although warm biases over the central-eastern Europe
755 increase with higher resolution, overall, ne30x8-t performs the best in terms of daily maximum
756 temperature extremes with the smallest RMSE values except in fall (when it has a similar RMSE
757 as in ne30x4-t). The largest improvement obtained by increasing resolution from 0.25° to 0.125°
758 is seen in DJF.

759



760

761 **Figure 11.** Distributions of the 99th percentile of daily Tmax from observations (CPC) (first
 762 column) and differences of simulations from observations. RMSEs are also given at the upper
 763 right of each panel. The observations and difference distributions use the lower and upper color
 764 bars, respectively.

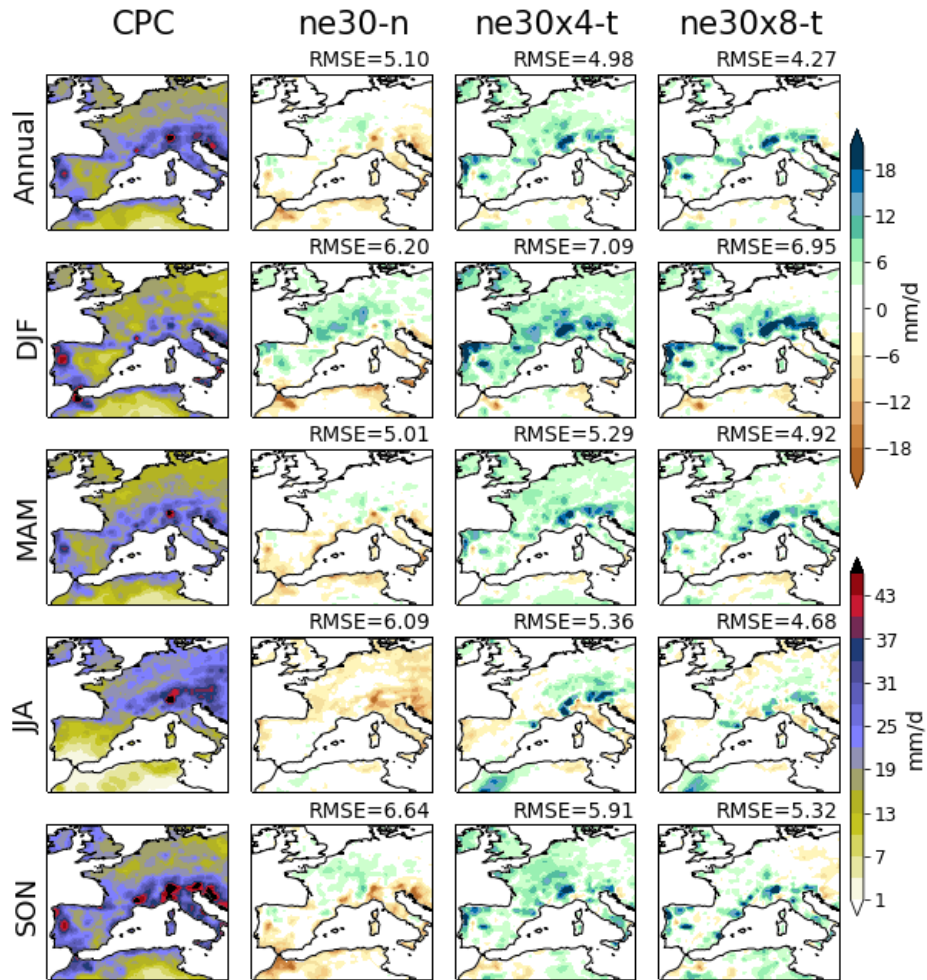
765 3.3.2 Extreme Precipitation

766 Figure S9 depicts the observed (CPC) spatial distributions of the 99th percentile
 767 thresholds for daily precipitation over the study domain. The highest threshold values, well
 768 exceeding 80 mm/d, occur over high elevations (e.g., the Atlas Mountains, the European Alps,
 769 the Dinaric Alps, the Apennines, and the Zagros Mountains) as well as at the west coasts (e.g.,
 770 the west coasts of Iberian Peninsula, Northern Africa, Croatia, and Anatolia) indicating the
 771 prominent influence of orography. There are apparently smaller precipitation rates (< 2 mm/d)
 772 over most of the southern regions (i.e., Northern Africa) consistent with this region's being
 773 located near the latitude belt of the descending branch of the Hadley cell.

774 In agreement with the previous studies which investigate extreme precipitation events in
 775 the Mediterranean region (e.g., Cavicchia et al., 2018; Dayan et al., 2015; Mastrantonas et al.,
 776 2020), western and eastern parts of the domain have different seasonalities, such that, the highest
 777 thresholds for the 99th percentile of daily precipitation are during fall and winter over the west

778 and east regions, respectively. As discussed in these studies, different physical mechanisms lead
779 to extreme precipitation events in different parts of the domain. The reader is referred to the
780 study by Dayan et al. (2015) for a review of large-scale circulation and regional to local
781 thermodynamic conditions leading to extreme precipitation events over the region. These
782 mechanisms include several atmospheric processes at different atmospheric scales, such as local
783 convection, upper synoptic-scale-level troughs, and mesoscale convective systems.

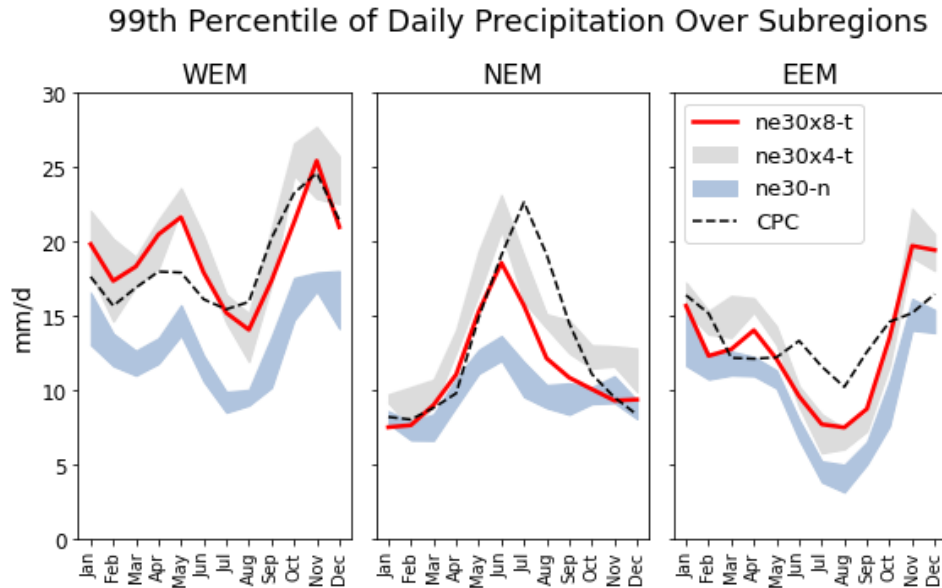
784 While temperature data are much more homogeneous in space and time, precipitation
785 data comprise strong spatiotemporal heterogeneity. Uncertainties related to evaluation data such
786 as the lack of enough stations over certain regions and observational undercatch caused by wind
787 effect particularly for solid precipitation (Rasmussen et al., 2012) further compromise the
788 inferences for model evaluations, even more so for the extreme precipitation. Hence, for a more
789 robust interpretation, the effects of increased resolution on the representation of extreme
790 precipitation are evaluated against two different datasets: CPC and E-OBS. Figure 12 and Figure
791 S10 show the observed spatial distributions of the 99th percentile thresholds of daily
792 precipitation and differences of the simulations from these observations over a region
793 encompassing western Europe and Northwestern Africa. This subregion is used here because it
794 includes high thresholds of extreme precipitation and has a complex topography. Furthermore, it
795 has a relatively high density of stations especially for E-OBS. Based on the RMSE values in
796 Figure 12, both VR simulations outperform the quasi-uniform 1° one in summer and fall and
797 0.125° resolution simulation (ne30x8-t) outperforms the 0.25° one in all seasons. Added value of
798 increasing resolution is apparent in the representation of summer extreme precipitation (RMSE
799 values are 6.09, 5.36, and 4.68 and 6.36, 5.63, and 5.02 mm/d for ne30-n, ne30x4-t, and ne30x8-
800 t, respectively). ne30x8-t has the smallest biases in summer among all model simulations. In
801 ne30x4-t and ne30x8-t, wet biases over high mountains including the Pyrennes and the European
802 Alps very likely exist due to systematic dry bias in the observations over high elevations which
803 significantly undermine an accurate assessment of improvements with high resolution by
804 artificially worsening the RMSE values (particularly in DJF). This is also supported by the lack
805 of such high wet biases for ne30-n highly possibly due to its smoother topography resolved
806 compared to VR configurations which decreases the duration snow cover persists. Even so, the
807 effect of increased resolution is clearly seen.



808

809 **Figure 12.** Distributions of the 99th percentile of daily precipitation from observations (CPC)
 810 (first column) and differences of simulations from observations (other columns) annually (first
 811 row) and seasonally (other rows). The observations and difference distributions use the lower
 812 and upper color bars, respectively.

813 Figure 13 displays the annual variability of extreme precipitation corresponding to the
 814 99th percentile of daily precipitation, averaged over the subregions WEM, NEM, and EEM (see
 815 Figure 2). The grey and blue shadings correspond to the ensemble spread of ne30x4-t and ne30-
 816 n, respectively. The ensemble spread of ne30x4-t generally does not overlap with that of ne30-n
 817 (except in February for NEM and in January for EEM) which indicates that increasing resolution
 818 from 1° to 0.25° leads to a substantially different climate in terms of extreme precipitation.
 819 Single ne30x8-t simulation shows some values outside of the ensemble spread of ne30x4-t,
 820 indicating that much higher resolution is able to produce a relatively different climate in terms of
 821 extreme precipitation events. For a smaller percentile (i.e., 0.95), there is no such clear separation
 822 of 1° and 0.25° ensembles and no apparent departure of 0.125° simulation from the ensemble
 823 spread of 0.25° resolution (Figure S11). Therefore, these results suggest that increased resolution
 824 has greater implications for the very heavy precipitation events, i.e., at the 99th percentile as
 825 shown here.



826

827 **Figure 13** Annual cycles of the 99th percentile of daily precipitation over the subregions of
 828 WEM, NEM, and EEM. Grey and blue shadings correspond to the ensemble spread of ne30x4-t
 829 and ne30-n, respectively. The red line is for the single ne30x8-t simulation.

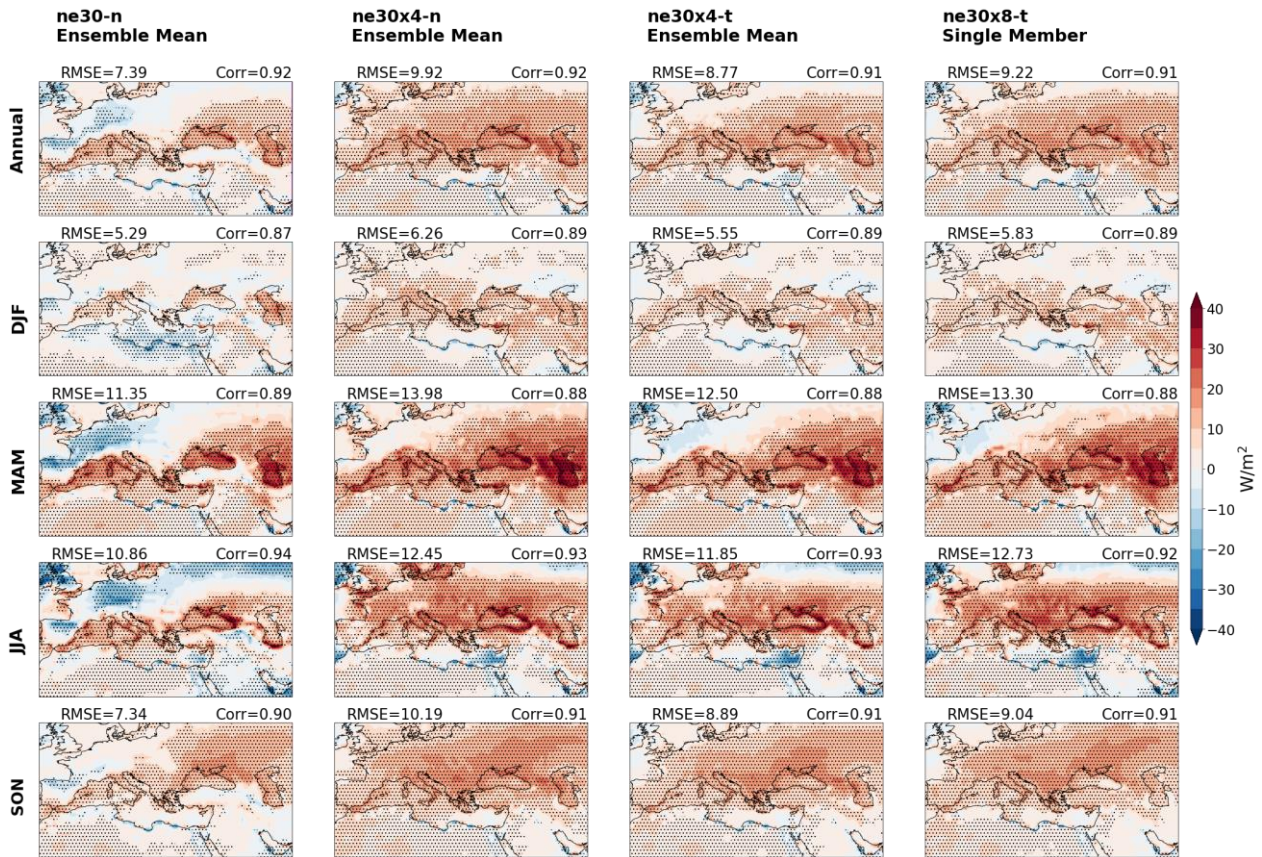
830 Over western Europe (WEM), simulated extreme precipitation has two maximums, one
 831 (the lower maximum) during May and the other during November-December. The shape of
 832 simulated seasonal cycles in this region are similar to that of observation, whereas the difference
 833 of precipitation amounts between two maximums are larger for observations. Over eastern
 834 Europe (NEM), a distinct seasonality is present with summer being the season with the highest
 835 extreme precipitation amounts suggesting the dominance of convective processes in producing
 836 extreme precipitation in this area. This conclusion is also consistent with the more apparent
 837 departure of ne30x8-t simulation from the ne30x4-t ensemble among all subregions very likely
 838 because of the distinctive skill of ne30x8-t in resolving small-scale processes such as convection.
 839 Here, the reduction in the activity of convective scheme with increased resolution should be
 840 recalled which most likely prevents to see the actual improvement obtained with high resolution.
 841 Over NEM, the shape of annual cycle is better reproduced by VR simulations than the control
 842 simulation with a maximum during summertime while the control simulation has a smaller
 843 maximum during November. Over this subregion, the observed maximum occurs slightly later,
 844 during July. Over EEM, all simulations reproduce a similar shaped seasonal cycle with
 845 maximums during April and November and a minimum during July-August. Observed minimum
 846 is also seen in August. However, the shapes of simulated seasonal cycles are different from the
 847 observed one.

848 3.4 Impacts of Tuning

849 Figure 14 shows the differences of the simulations from observations (CERES EBAF) for
 850 SWCF annually and seasonally. Pattern correlations are between 0.87-0.94. The biases of Top of
 851 Atmosphere (TOA) shortwave cloud forcings remarkably worsen in ne30x4-n compared to ne30-
 852 n with the following RMSE values (in W/m^2): Annual: 7.39 vs. 9.92, DJF: 5.29 vs. 6.26, MAM:
 853 11.35 vs. 13.98, JJA: 10.86 vs. 12.45, and SON: 7.34 vs. 10.19, respectively. With increased
 854 resolution, most prominent changes in the biases are the decrease in the area of the regions where

855 SWCF is underestimated by the model (e.g., Northwestern Europe, Central and Eastern Anatolia,
 856 the Arabian Peninsula) and expansion in the area overestimated with higher amplitudes (e.g.,
 857 North of the Mediterranean Sea, the Black Sea, and the Caspian Sea) due to too thin clouds.
 858 Increasing horizontal resolution and/or reducing the physics time-step tends to thin the clouds,
 859 leading to a positive TOA energy imbalance (Herrington et al. 2022; Wijngaard et al. 2023).
 860 Parameter tuning was used to thicken the clouds in our VR simulations.

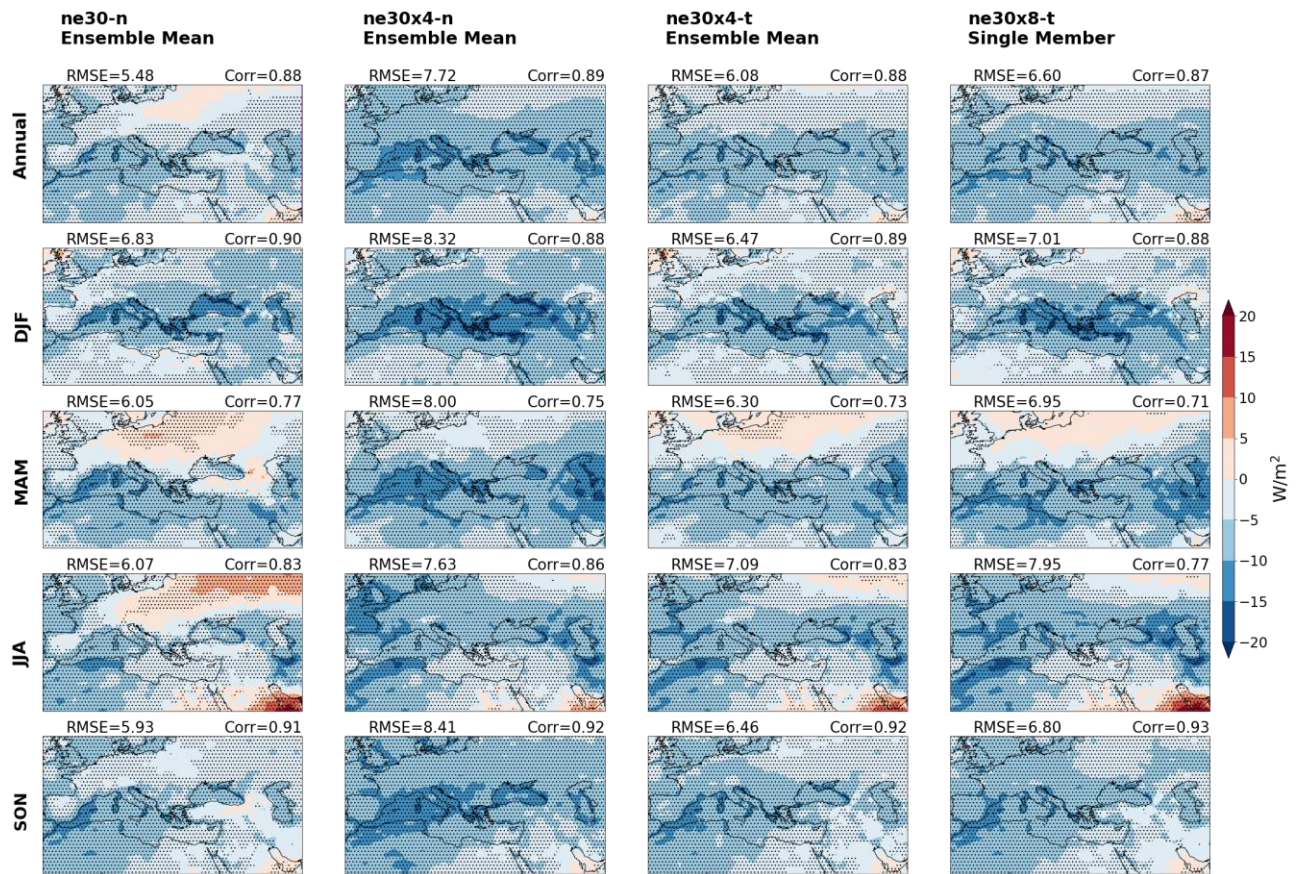
861



862

863 **Figure 14.** Annual (first row) and seasonal (other rows) differences of SWCF between
 864 simulations (ne30-n, ne30x4-n, ne30x4-t, and ne30x8-t in order) and observations. The
 865 observations are from CERES EBAF. RMSE and pattern correlations are given at the top of each
 866 panel. The dots indicate areas where the differences are statistically significant at the 95% level
 867 based on a two-sided Student's t-test.

868 Figure 15 shows the differences of the simulations from observations (CERES EBAF) for
 869 LWCF annually and seasonally. Pattern correlations are 0.71-0.93, slightly lower than that for
 870 SWCF. The biases of TOA longwave cloud forcings worsen in ne30x4-n compared to ne30-n
 871 with the following RMSE values (in W/m^2): Annual: 5.48 vs. 7.72, DJF: 6.83 vs. 8.32, MAM:
 872 6.05 vs. 8.00, JJA: 6.07 vs. 7.63, and SON: 5.93 vs. 8.41, respectively. With increased resolution
 873 the area of the regions overestimated by the model (e.g., Central and Eastern Europe, Northeast
 874 of Anatolia, East of the Arabian Peninsula over the Persian Gulf) decreases and the areas
 875 underestimated (e.g., North of the Mediterranean Sea, the Black Sea, and the Caspian Sea in
 876 DJF, Northwest of Africa in SON) expands.



877

878 **Figure 15.** Same as Figure 14 but for LWCF.

879 With tuning, we target obtaining TOA longwave and shortwave radiation values which
 880 are in better agreement with observations (CERES EBAF dataset). We focus on the cloud
 881 forcing terms to investigate how tuning impacts the radiative effects of clouds. Although
 882 generally similar bias patterns remain, ne30x4-t simulations obtained by applying parameter
 883 tunings to ne30x4-n show improvements in the representation of SWCF and LWCF (check the
 884 columns 2 and 3 in Figures 14 and 15). With tuning, the signs and amplitudes of biases are
 885 restored to those in ne30-n to some degree. On the other hand, when resolution is increased
 886 more from ne30x4-t to ne30x8-t, the RMSE values increase again although both simulations use
 887 identical tunings. This suggests that extra tunings are needed after increasing horizontal
 888 resolution further to recover this deterioration.

889 4 Conclusions

890 The primary objective of this study is to evaluate the performance of VR-CESM
 891 historical experiments in simulating the mean climatology and seasonal variability of surface
 892 temperature and precipitation over the Euro-Mediterranean region. The evaluation has been
 893 carried out by comparing variable resolution simulations with the quasi-uniform 1° control
 894 simulation and against observational and reanalysis datasets. This study also aims to explain the
 895 reasons for persistent biases in the simulations to guide better interpretation of results. The
 896 impacts of parameter tunings applied to the 0.25° VR simulation are also discussed with respect
 897 to changes in the longwave and shortwave cloud forcings.

898 Overall, VR simulations show more accurate representation of surface temperature and
899 precipitation mainly due to better representations of topographical variance, including steep
900 orographical gradients and land-sea contrasts, and of fine-scale processes such as orographic
901 uplift and convection. The locations and expansions of upward and downward air motions are
902 better simulated with high resolution, consistent with prior VR-CESM studies (Herrington et al.,
903 2022; Morris et al., 2023). Therefore, added value of increased resolution is most evident at
904 mountainous and coastal regions and for higher-moment climate statistics such as extreme
905 events.

906 1° coarse resolution has large area-averaged surface temperature biases of approximately
907 2°C or more with the largest biases occurring in winter. There exist much higher warm biases
908 over high mountains and coastal areas exceeding $+6^\circ\text{C}$ locally and in different seasons. With the
909 resolution increased to 0.25° , biases significantly reduce particularly over areas with strong
910 spatial gradients. These reductions clearly show the added-value of better topographic
911 representation at higher resolutions. Simply increasing the resolution from 0.25° to 0.125° leads
912 to further improvements, but not as much as seen upon increasing it from 1° to 0.25° , almost
913 certainly because the topographical representations at 0.25° and 0.125° are quite similar whereas
914 those of 1° are heavily smoothed. Still, 0.125° simulation shows the smallest temperature biases
915 in all seasons in all the simulations.

916 Simulation of precipitation is more complicated than that of temperature because
917 precipitation occurs as a result of many subgrid scale processes and accordingly its higher
918 parameter dependency results in more uncertainty. On the other hand, increasing resolution from
919 1° to 0.25° improves the model performance. For precipitation, added value of increased
920 resolution, again, is clearly seen in the areas with complex topography. Particularly, the
921 reduction in precipitation biases on the windward/leeward sides of high mountains and on the
922 coasts is a demonstration of higher skill of increased resolution in resolving adjacent
923 topographical gradients and coastlines. Further increasing the resolution to 0.125° reduces the
924 summertime biases whereas the biases in other seasons get slightly worse, mostly because of the
925 lack of extra parameter tunings. Better summertime performance of 0.125° can be attributed to
926 its ability to resolve more smaller scale processes related to convective activity.

927 Despite improvements, there are persistent temperature and precipitation biases across all
928 simulations. We see a general warm (cold) bias over the northern (southern) areas of the region
929 and a warm-dry bias over central and eastern Europe. These bias patterns are mainly related to
930 land-atmosphere interactions. Another persistent bias is the overestimation of precipitation over
931 northwest Europe especially in winter. High-resolution simulations show smaller winter wet
932 biases than 1° control simulation in this region. This can be attributed to better representation of
933 water vapor transport from the North Atlantic, as a demonstration of the ability of increased
934 resolution in resolving dynamical processes driving precipitation, and also as a result of better
935 topographical treatment which is more skillful in resolving orographic uplift on the windward
936 side of the European Alps.

937 The added value of increased resolution is clearly evident in the representation of
938 extreme maximum temperatures and precipitation. Generally, 0.25° resolution performs better
939 than 1° and 0.125° resolution performs the best in terms of daily maximum temperature
940 extremes. 0.25° resolution produces a different climate than 1° with respect to 99th percentile

941 precipitation and 0.125° has the smallest biases in summer among all the simulations, consistent
942 with the dominance of small scale processes in this season.

943 The results obtained by doubling the horizontal resolution from 0.25° to 0.125° should be
944 interpreted cautiously. First, this simulation consists of a single run and is not an ensemble as in
945 other simulations. So, the uncertainties caused by internal variability still exist without an
946 ensemble size large enough to produce a sufficient statistical sample. Internal variability
947 becomes increasingly important for processes occurring at smaller spatiotemporal scales
948 including the extreme events. Because, at small scales an additional spatial heterogeneity is
949 introduced leading to an additional internal variability which is partly averaged out at large
950 scales (Aalbers et al. 2018). Second, no specific tunings were applied over the 0.25° version
951 although timestep has been reduced. Therefore, the improvements seen are related to simply
952 increasing the horizontal resolution and further potential improvements are very likely offset by
953 lack of extra tunings. Third, 0.125° resolution has a topographical representation very similar to
954 that of 0.25° , therefore we should not expect additional improvements in the topography-induced
955 processes which can already be resolved by 0.25° . Even so, 0.125° simulation gives a clear
956 evidence of potential for further improvements in higher resolutions.

957 Shortwave and longwave cloud forcing biases that increase as a result of increasing
958 resolution from 1° to 0.25° are apparently corrected with tuning to some degree. However,
959 further increasing the resolution to 0.125° causes biases to get slightly worse again. Parameter
960 tunings do not result in a general improvement in the representation of surface temperature and
961 precipitation, as they target the cloud radiative forcing.

962 Significant difficulties arise in the interpretation of simulation results because of the
963 region's very complicated topography and climatologically different zones it encompasses.
964 Equally important is the fact that default model parameterizations are developed for use in coarse
965 resolution simulations, thus increasing resolution and accordingly decreasing the timestep lead to
966 some artificial biases including those caused by the reduction in the activity of the convective
967 scheme. Another source of artificial error, such as vastly overestimated precipitation over high
968 elevations with increased resolution, is due to deficiencies of the observational datasets. With the
969 caveat that the results must be interpreted cautiously, overall, variable resolution simulations
970 improve the representation of spatial distributions and seasonal evolution of T2m and
971 precipitation as well as the extreme precipitation and heat events over the Euro-Mediterranean
972 region. This makes VR-CESM a useful tool for evaluating the regional climate at high resolution
973 and for employing it for climate change studies for the region.

974

975

976

977

978

979

980

981 **Acknowledgments**

982 This study was supported by the 2247A National Outstanding Researchers Program of the
983 Scientific and Technological Research Council of Türkiye (TUBITAK) under grant 120C137.
984 The financial support from TUBITAK does not mean that the content of the publication reflects
985 the approved scientific view of TUBITAK. Computer resources of the National Center for High
986 Performance Computing of Türkiye (UHeM) (under grant number 1006542019) was used to
987 simulate runs and analyze the data for this research. This material is also based upon work
988 supported by the U.S. National Science Foundation (NSF) National Center for Atmospheric
989 Research (NCAR), which is a major facility sponsored by the U.S. NSF under Cooperative
990 Agreement 1852977. Some of the simulations were performed on the Cheyenne Supercomputer
991 (doi:10.5065/D6RX99HX) at the NSF NCAR – Wyoming Supercomputing Center during Burcu
992 Boza’s visit to the NSF NCAR on the TUBITAK fellowship. The study was partly funded by the
993 Scientific and Technological Research Council of Türkiye (TUBITAK) via an International
994 Research Fellowship Programme for PhD Students (2214-A).

995

996 **Open Research**

997 The observation and reanalysis data sets used in this study are publicly available at their source
998 repositories. The CPC Global Unified Gauge-Based Analysis of Daily Precipitation and CPC
999 Global Unified Temperature data were provided by the NOAA PSL, Boulder, Colorado, USA,
1000 from their website at <https://psl.noaa.gov>. The CESM2.2 code is available
1001 at <https://github.com/ESCOMP/CESM>. Analyses are performed and figures are created by using
1002 Python (v3.8.13). The raw simulation data for the variables used to generate the figures are made
1003 available at Zenodo (DOIs: 10.5281/zenodo.10899785, 10.5281/zenodo.10916689,
1004 10.5281/zenodo.10916873, 10.5281/zenodo.10928100, 10.5281/zenodo.10928245,
1005 10.5281/zenodo.10928269, 10.5281/zenodo.10928342, 10.5281/zenodo.10929045,
1006 10.5281/zenodo.10929342, 10.5281/zenodo.10929377, 10.5281/zenodo.10929387).

1007

1008

1009

1010

1011

1012

1013

1014

1015

1016

1017 **References**

- 1018 Aalbers, E., Lenderink, G., Meijgaard, E., & Hurk, B. (2018). Local-scale changes in mean and heavy precipitation
1019 in Western Europe, climate change or internal variability?. *Climate Dynamics*, 50. [https://doi.org/10.1007/s00382-](https://doi.org/10.1007/s00382-017-3901-9)
1020 [017-3901-9](https://doi.org/10.1007/s00382-017-3901-9)
- 1021 Abiodun, B., Prusa, J., & Gutowski, W. (2008). Implementation of a non-hydrostatic, adaptive-grid dynamics core
1022 in CAM3. Part I: Comparison of dynamics cores in aqua-planet simulations. *Climate Dynamics*, 31, 795-810.
1023 <https://doi.org/10.1007/s00382-008-0381-y>
- 1024 Bacmeister, J. T., Lauritzen, P. H., Dai, A., & Truesdale, J. E. (2012), Assessing possible dynamical effects of
1025 condensate in high resolution climate simulations, *Geophysical Research Letters*, 39, L04806.
1026 <https://doi.org/10.1029/2011GL050533>
- 1027 Batibeniz, F., Ashfaq, M., Onol, B., Turuncoglu, U., Mehmood, S., & Evans, K. (2020). Identification of major
1028 moisture sources across the Mediterranean Basin. *Climate Dynamics*, 54, 1-19. [https://doi.org/10.1007/s00382-020-](https://doi.org/10.1007/s00382-020-05224-3)
1029 [05224-3](https://doi.org/10.1007/s00382-020-05224-3)
- 1030 Bergant, K., Belda, M., & Halenka, T. (2007). Systematic errors in the simulation of European climate (1961-2000)
1031 with RegCM3 driven by NCEP/NCAR reanalysis. *International Journal of Climatology*, 27, 455 - 472.
1032 <https://doi.org/10.1002/joc.1413>
- 1033 Bogenschütz, P. A., Gettelman, A., Hannay, C., Larson, V. E., Neale, R. B., Craig, C., & Chen, C.-C. (2018). The
1034 path to CAM6: Coupled simulations with CAM5.4 and CAM5.5. *Geoscientific Model Development*, 11(1), 235–
1035 255. <https://doi.org/10.5194/gmd-11-235-2018>
- 1036 Bozkurt, D., Ezber, Y., & Sen, O. (2019). Role of the East Asian trough on the eastern Mediterranean temperature
1037 variability in early spring and the extreme case of 2004 warm spell. *Climate Dynamics*.
1038 <https://doi.org/10.1007/s00382-019-04847-5>
- 1039 Bozkurt, D., Turuncoglu, U., Sen, O., Onol, B., & Dalfes, N. (2012). Downscaled simulations of the ECHAM5,
1040 CCSM3 and HadCM3 global models for the eastern Mediterranean-Black Sea region: Evaluation of the reference
1041 period. *Climate Dynamics*, 39, 207-225. <https://doi.org/10.1007/s00382-011-1187-x>
- 1042 Briegleb, B. P., & Light, B. (2007). A Delta-Eddington Multiple Scattering Parameterization for Solar Radiation in
1043 the Sea Ice Component of the Community Climate System Model (No. NCAR/TN-472+STR). University
1044 Corporation for Atmospheric Research. <https://doi.org/10.5065/D6B27S71>
- 1045 Cavicchia, L., Scoccimarro, E., Gualdi, S., Marson, P., Ahrens, B., Berthou, S., et al. (2018). Mediterranean extreme
1046 precipitation: a multi-model assessment. *Climate Dynamics*, 51, 901–913. [https://doi.org/10.1007/s00382-016-3245-](https://doi.org/10.1007/s00382-016-3245-x)
1047 [x](https://doi.org/10.1007/s00382-016-3245-x)
- 1048 Chen, S.-C. (2002). Model mismatch between global and regional simulations. *Geophysical Research Letters*, 29(5).
1049 <https://doi.org/10.1029/2001GL013570>
- 1050 Chen, M., Shi, W., Xie, P., Silva, V., Kousky, V., Higgins, W., & Janowiak, J. (2008). Assessing objective
1051 techniques for gauge-based analyses of global daily precipitation. *Journal of Geophysical Research (Atmospheres)*,
1052 113, 4110-. <https://doi.org/10.1029/2007JD009132>
- 1053 Cornes, R. C., van der Schrier, G., van den Besselaar, E. J. M., & Jones, P. D. (2018). An ensemble version of the E-
1054 OBS temperature and precipitation data sets. *Journal of Geophysical Research: Atmospheres*, 123, 9391–
1055 9409. <https://doi.org/10.1029/2017JD028200>
- 1056 Dafka, S., Xoplaki, E., Toreti, A., Zanis, P., Tyrlis, E., Zerefos, C., & Luterbacher, J. (2016). The Etesians: from
1057 observations to reanalysis. *Climate Dynamics*, 47. <https://doi.org/10.1007/s00382-015-2920-7>
- 1058 Danabasoglu, G., Lamarque, J.-F., Bacmeister, J., Bailey, D. A., DuVivier, A. K., Edwards, J., et al. (2020). The
1059 Community Earth System Model Version 2 (CESM2). *Journal of Advances in Modeling Earth Systems*, 12,
1060 e2019MS001916. <https://doi.org/10.1029/2019MS001916>

- 1061 Danielson, J.J., & Gesch, D.B. (2011). Global multi-resolution terrain elevation data 2010 (GMTED2010): U.S.
1062 Geological Survey Open-File Report, 2011–1073, 26 p. <https://doi.org/10.3133/ofr20111073>
- 1063 Dayan, U., Nissen, K., & Ulbrich, U. (2015). Review Article: Atmospheric conditions inducing extreme
1064 precipitation over the eastern and western Mediterranean. *Natural Hazards and Earth System Sciences*, 15.
1065 <https://doi.org/10.5194/nhess-15-2525-2015>
- 1066 Dennis, J.M., Edwards, J., Evans, K.J., Guba, O., Lauritzen, P.H., Mirin, A.A., et al. (2012). CAM-SE: A scalable
1067 spectral element dynamical core for the Community Atmosphere Model. *The International Journal of High
1068 Performance Computing Applications*, 26, 74 - 89. <https://doi.org/10.1177/1094342011428142>
- 1069 Di Luca, A., Argüeso, D., Sherwood, S., & Evans, J. P. (2021). Evaluating precipitation errors using the
1070 environmentally conditioned intensity-frequency decomposition method. *Journal of Advances in Modeling Earth
1071 Systems*, 13, e2020MS002447. <https://doi.org/10.1029/2020MS002447>
- 1072 Fan, F., Bradley, R., & Rawlins, M. (2014). Climate change in the northeastern US: Regional climate model
1073 validation and climate change projections. *Climate Dynamics*, 43. <https://doi.org/10.1007/s00382-014-2198-1>
- 1074 Feser, F., Rockel, B., Storch, H., Winterfeldt, J., & Zahn, M. (2011). Regional Climate Models Add Value to Global
1075 Model Data: A Review and Selected Examples. *Bulletin of the American Meteorological Society*, 92(9), 1181-1192.
1076 <https://doi.org/10.1175/2011BAMS3061.1>
- 1077 Fita, L., Romero, R., De Luque Söllheim, A., Emanuel, K., & Ramis, C. (2007). Analysis of the environments of
1078 seven Mediterranean tropical-like storms using an axisymmetric, nonhydrostatic, cloud resolving model. *Natural
1079 Hazards and Earth System Science*, 7. <https://doi.org/10.5194/nhess-7-41-2007>
- 1080 Flato, G., J. Marotzke, B. Abiodun, P. Braconnot, S.C. Chou, W. Collins, et al. (2013) Evaluation of Climate
1081 Models. In: Climate Change 2013: The Physical Science Basis. Contribution of Working Group I to the Fifth
1082 Assessment Report of the Intergovernmental Panel on Climate Change [Stocker, T.F., D. Qin, G.-K. Plattner, M.
1083 Tignor, S.K. Allen, J. Boschung, A. Nauels, Y. Xia, V. Bex and P.M. Midgley (eds.)]. Cambridge University Press,
1084 Cambridge, United Kingdom and New York, NY, USA.
- 1085 Fox-Rabinovitz, M., Côté, J., Dugas, B., Déqué, M., & McGregor, J. L. (2006) Variable resolution general
1086 circulation models: Stretched-grid model intercomparison project (SGMIP), *Journal of Geophysical Research*, 111,
1087 D16 104, <https://doi.org/10.1029/2005JD006520>
- 1088 Gettelman, A., Callaghan, P., Larson, V. E., Zarzycki, C. M., Bacmeister, J. T., Lauritzen, P. H., et al.
1089 (2018). Regional climate simulations with the Community Earth System Model. *Journal of Advances in Modeling
1090 Earth Systems*, 10, 1245–1265. <https://doi.org/10.1002/2017MS001227>
- 1091 Gettelman, A., Mills, M. J., Kinnison, D. E., Garcia, R. R., Smith, A. K., Marsh, D. R., et al. (2019). The whole
1092 atmosphere community climate model version 6 (WACCM6). *Journal of Geophysical Research:
1093 Atmospheres*, 124, 12380–12403. <https://doi.org/10.1029/2019JD030943>
- 1094 Gettelman, A., & Morrison, H.. (2015). Advanced Two-Moment Bulk Microphysics for Global Models. Part I: Off-
1095 Line Tests and Comparison with Other Schemes. *Journal of Climate*, 28, 1268-1287. <https://doi.org/10.1175/JCLI-D-14-00102.1>
- 1097 Giorgi F. (2006) Climate change hot-spots. *Geophysical Research Letters*, 33:L08707.
1098 <https://doi.org/10.1029/2006GL025734>
- 1099 Giorgi, F., Bi, X. & Pal, J.S. (2004). Mean, interannual variability and trends in a regional climate change
1100 experiment over Europe. I. Present-day climate (1961–1990). *Climate Dynamics*, 22, 733–756.
1101 <https://doi.org/10.1007/s00382-004-0409-x>
- 1102 Golaz, J.-C., Larson, V. E., & Cotton, W. R. (2002) A PDF-Based Model for Boundary Layer Clouds. Part I:
1103 Method and Model Description. *Journal of the Atmospheric Sciences*, vol. 59, no. 24, 3540–3551.
1104 [https://doi.org/10.1175/1520-0469\(2002\)059<3540:APBMFB>2.0.CO;2](https://doi.org/10.1175/1520-0469(2002)059<3540:APBMFB>2.0.CO;2)
- 1105 Guba, O., Taylor, M., Ullrich, P., Overfelt, J., & Levy, M. (2014). The spectral element method (SEM) on variable-
1106 resolution grids: Evaluating grid sensitivity and resolution-aware numerical viscosity. *Geoscientific Model
1107 Development Discussions*, 7. <https://doi.org/10.5194/gmdd-7-4081-2014>

- 1108 Guo, Z., M. Wang, Y. Qian, V. E. Larson, S. Ghan, M. Ovchinnikov, et al. (2015). Parametric behaviors of CLUBB
 1109 in simulations of low clouds in the Community Atmosphere Model (CAM), *Journal of Advances in Modeling Earth*
 1110 *Systems*, 7, 1005–1025, <https://doi.org/10.1002/2014MS000405>
- 1111 Gutowski, W., Ullrich, P., Hall, A., Leung, L., O'Brien, T., Patricola, C., et al. (2020). The Ongoing Need for High-
 1112 Resolution Regional Climate Models: Process Understanding and Stakeholder Information. *Bulletin of the American*
 1113 *Meteorological Society* 101. <https://doi.org/10.1175/BAMS-D-19-0113.1>
- 1114 Harris, I., Jones, P.D., Osborn, T.J., & Lister, D.H. (2014). Updated high-resolution grids of monthly climatic
 1115 observations – the CRU TS3.10 Dataset. *International Journal of Climatology*, 34, 623-
 1116 642. <https://doi.org/10.1002/joc.3711>
- 1117 Harris, I., Osborn, T., Jones, P., & Lister, D. (2020). Version 4 of the CRU TS monthly high-resolution gridded
 1118 multivariate climate dataset. *Scientific Data*, 7. <https://doi.org/10.1038/s41597-020-0453-3>
- 1119 Herrington, A. R., Lauritzen, P. H., Lofverstrom, M., Lipscomb, W. H., Gettelman, A., & Taylor, M. A. (2022).
 1120 Impact of grids and dynamical cores in CESM2.2 on the surface mass balance of the Greenland Ice Sheet. *Journal of*
 1121 *Advances in Modeling Earth Systems*, 14, e2022MS003192. <https://doi.org/10.1029/2022MS003192>
- 1122 Herrington, A., Lauritzen, P., Reed, K., Goldhaber, S., & Eaton, B. (2019). Exploring a lower resolution physics
 1123 grid in CAM-SE-CSLAM. *Journal of Advances in Modeling Earth Systems*, 11.
 1124 <https://doi.org/10.1029/2019MS001684>
- 1125 Herrington, A. & Reed, K. (2017). An Explanation for the Sensitivity of the Mean State of the Community
 1126 Atmosphere Model to Horizontal Resolution on Aquaplanets. *Journal of Climate*, 30. <https://doi.org/10.1175/JCLI-D-16-0069.1>
- 1128 Herrington, A. R., & Reed, K. A. (2020). On resolution sensitivity in the Community Atmosphere Model. *Quarterly*
 1129 *Journal Of The Royal Meteorological Society*, 146, 3789-3807. <https://doi.org/10.1002/qj.3873>
- 1130 Hersbach, H., Bell, B., Berrisford, P., Hirahara, S., Horányi, A., Muñoz Sabater, J., et al. (2020). The ERA5 global
 1131 reanalysis. *Quarterly Journal of the Royal Meteorological Society*. <https://doi.org/10.1002/qj.3803>
- 1132 Huang, X., Rhoades, A. M., Ullrich, P. A., & Zarzycki, C. M. (2016). An evaluation of the variable-resolution-
 1133 CESM for modeling California's climate, *Journal of Advances in Modeling Earth Systems*, 8, 345–369, <https://doi.org/10.1002/2015MS000559>
- 1135 Hunke, E. C., Lipscomb, W. H., Turner, A. K., Jeffery, N., & Elliott, S. (2015). CICE: The Los Alamos Sea Ice
 1136 Model Documentation and Software User's Manual Version 5.1. T-3 Fluid Dynamics Group, Los Alamos National
 1137 Laboratory, Tech. Rep. LA-CC-06-012.
- 1138 Hurrell, J.W., Hack, J., Shea, D., Caron, J., & Rosinski, J. (2008). A New Sea Surface Temperature and Sea Ice
 1139 Boundary Dataset for the Community Atmosphere Model. *Journal of Climate*, 21. <https://doi.org/10.1175/2008JCLI2292.1>
- 1141 Insua-Costa, D., Senande-Rivera, M., Llasat, M.D., & Miguez-Macho, G. (2022). A global perspective on western
 1142 Mediterranean precipitation extremes. *npj Climate and Atmospheric Science*, 5, 1-7. <https://doi.org/10.1038/s41612-022-00234-w>
- 1144 Iturbide, M., Gutiérrez, J., Alves, L., Bedia, J., Cerezo-Mota, R., Gimeno, E., et al. (2020). An update of IPCC
 1145 climate reference regions for subcontinental analysis of climate model data: definition and aggregated datasets.
 1146 *Earth System Science Data*, 12, 2959-2970. <https://doi.org/10.5194/essd-12-2959-2020>
- 1147 Kato, S., Rose, F., Rutan, D., Thorsen, T., Loeb, N., Doelling, D., et al. (2018). Surface irradiances of edition 4.0
 1148 Clouds and the Earth's Radiant Energy System (CERES) Energy Balanced and Filled (EBAF) data product. *Journal*
 1149 *of Climate*, 31. <https://doi.org/10.1175/JCLI-D-17-0523.1>
- 1150 Kotlarski, S., Keuler, K., Christensen, O., Colette, A., Deque, M., Gobiet, A., et al. (2014). Regional climate
 1151 modeling on European scales: A joint standard evaluation of the EURO-CORDEX RCM ensemble. *Geoscientific*
 1152 *Model Development*, 7, 1297-1333. <https://doi.org/10.5194/gmd-7-1297-2014>
- 1153 Kotték, M., Grieser, J., Beck, C., Rudolf, B., & Rubel, F. (2006). World Map of the Köppen-Geiger climate
 1154 classification updated. *Meteorologische Zeitschrift*, 15:259-263. <https://doi.org/10.1127/0941-2948/2006/0130>

- 1155 Larson, V. E. (2017). CLUBB-SILHS: A parameterization of subgrid variability in the atmosphere.
 1156 arXiv:1711.03675v2 [physics.ao-ph]. <https://doi.org/10.48550/arXiv.1711.03675>
- 1157
- 1158 Lauritzen, P. H., Bacmeister, J. T., Callaghan, P. F., & Taylor, M. A. (2015). NCAR_Topo (v1.0): NCAR global
 1159 model topography generation software for unstructured grids. *Geoscientific Model Development*, 8(12), 3975–3986.
 1160 <https://doi.org/10.5194/gmd-8-3975-2015>
- 1161 Lauritzen, P. H., Nair, R. D., Herrington, A. R., Callaghan, P., Goldhaber, S., Dennis, J. M., et al. (2018). NCAR
 1162 release of CAM-SE in CESM2.0: A reformulation of the spectral element dynamical core in dry-mass vertical
 1163 coordinates with comprehensive treatment of condensates and energy. *Journal of Advances in Modeling Earth
 1164 Systems*, 10(7), 1537–1570. <https://doi.org/10.1029/2017MS001257>
- 1165 Lawrence, D. M., Fisher, R. A., Koven, C. D., Oleson, K. W., Swenson, S. C., Bonan, G., et al. (2019). The
 1166 Community Land Model version 5: Description of new features, benchmarking, and impact of forcing
 1167 uncertainty. *Journal of Advances in Modeling Earth Systems*, 11, 4245–
 1168 4287. <https://doi.org/10.1029/2018MS001583>
- 1169 Lin, Y., Dong, W., Zhang, M., Xie, Y., Xue, W., Huang, J., & Luo, Y. (2017). Causes of model dry and warm bias
 1170 over central U.S. and impact on climate projections. *Nature Communications*, 8. [https://doi.org/10.1038/s41467-
 1171 017-01040-2](https://doi.org/10.1038/s41467-017-01040-2)
- 1172 Lionello, P., Malanotte-Rizzoli, P., & Boscolo, R.(Eds). (2006). *Mediterranean Climate Variability* (pp 179–226).
 1173 Amsterdam, NETHERLANDS: Elsevier.
- 1174 Loeb, N., Doelling, D., Wang, H., Su, W., Nguyen, C., Corbett, J., et al. (2017). Clouds and the Earth's Radiant
 1175 Energy System (CERES) Energy Balanced and Filled (EBAF) top-of-atmosphere (TOA) edition-4.0 data product.
 1176 *Journal of Climate*, 31. <https://doi.org/10.1175/JCLI-D-17-0208.1>
- 1177 Mastrantonas, N., Herrera-Lormendez, P., Magnusson, L., Pappenberger, F. & Matschullat, J. (2020). Extreme
 1178 precipitation events in the Mediterranean: Spatiotemporal characteristics and connection to large-scale atmospheric
 1179 flow patterns. *International Journal of Climatology*, 41, 4, 2710–2728. <https://doi.org/10.1002/joc.6985>
- 1180 Matte, D., Laprise, R., Thériault, J. M., & Lucas-Picher, P. (2017). Spatial spin-up of fine scales in a regional
 1181 climate model simulation driven by low-resolution boundary conditions. *Climate Dynamics*, 49(1–2), 563–574.
 1182 <https://doi.org/10.1007/s00382-016-3358-2>
- 1183 Mauritsen, T., Stevens, B., Roeckner, E., Crueger, T., Esch, M., Giorgetta, M., et al. (2012). Tuning the climate of a
 1184 global model. *Journal of Advances in Modeling Earth Systems*, 4. <https://doi.org/10.1029/2012MS000154>
- 1185 McGregor, J. L. and Dix, M. R.: An updated description of the Conformal-Cubic Atmospheric Model (2008), in:
 1186 High Resolution Numerical Modelling of the Atmosphere and Ocean, edited by: Hamilton, K. and Ohfuchi, W.,
 1187 Springer, New York, USA, 51– 76. https://doi.org/10.1007/978-0-387-49791-4_4
- 1188 Morris, M., Kushner , P. J., Moore , G. W. K., & Mercan , O. M. (2023) Atmospheric Circulation Patterns
 1189 Associated with Extreme Wind Events in Canadian Cities. *Journal of Climate*, 36, 4443–4460.
 1190 <https://doi.org/10.1175/JCLI-D-22-0719.1>
- 1191 Mueller, B., & Seneviratne, S. (2014). Systematic land climate and evapotranspiration biases in CMIP5 simulations:
 1192 CMIP5 BIASES. *Geophysical Research Letters*, 41. <https://doi.org/10.1002/2013GL058055>
- 1193 Onol, B., & Semazzi, F. (2009). Regionalization of Climate Change Simulations over the Eastern Mediterranean.
 1194 *Journal of Climate*, 22,1944–1961. <https://doi.org/10.1175/2008JCLI1807.1>
- 1195 Räisänen, J., Hansson, U., Ullerstig, A., Döscher, R., Graham, L., Jones, C., et al. (2004). European climate in the
 1196 late twenty-first century: Regional simulations with two driving global models and two forcing scenarios. *Climate
 1197 Dynamics*, 22, 13–31. <https://doi.org/10.1007/s00382-003-0365-x>
- 1198 Rahimi, S. R., Wu, C., Liu, X., & Brown, H. (2019). Exploring a variable-resolution approach for simulating
 1199 regional climate over the Tibetan Plateau using VR-CESM. *Journal of Geophysical Research:*
 1200 *Atmospheres*, 124, 4490–4513. <https://doi.org/10.1029/2018JD028925>

- 1201 Rasmussen, R., Baker, B., Kochendorfer, J., Meyers, T. Landolt, S., Fischer, A., et al. (2012). How well are we
 1202 measuring snow: the NOAA/FAA/NCAR winter precipitation test bed. *Bulletin of the American Meteorological*
 1203 *Society*, 93. <https://doi.org/10.1175/BAMS-D-11-00052.1>
- 1204 Reed, K., Jablonowski, C., & Taylor, M. (2012). Tropical cyclones in the spectral element configuration of the
 1205 Community Atmosphere Model. *Atmospheric Science Letters*, 13, 303-310. <https://doi.org/10.1002/asl.399>
- 1206 Rhoades, A., Huang, X., Ullrich, P., & Zarzycki, C. (2015). Characterizing Sierra Nevada Snowpack Using
 1207 Variable-Resolution CESM. *Journal of Applied Meteorology and Climatology*, 55, 151023111431006.
 1208 <https://doi.org/10.1175/JAMC-D-15-0156.1>
- 1209 Rhoades, A., Jones, A., Srivastava, A., Huang, H., O'Brien, T., Patricola, C., et al. (2020). The Shifting Scales of
 1210 Western US Landfalling Atmospheric Rivers Under Climate Change. *Geophysical Research Letters*, 47.
 1211 <https://doi.org/10.1029/2020GL089096>
- 1212 Rhoades, A., Ullrich, P., Zarzycki, C., Johansen, H., Margulis, S., Morrison, et al. (2018). Sensitivity of Mountain
 1213 Hydroclimate Simulations in Variable-Resolution CESM to Microphysics and Horizontal Resolution. *Journal of*
 1214 *Advances in Modeling Earth Systems*. <https://doi.org/10.1029/2018MS001326>
- 1215 Ringler, T., Jacobsen, D., Gunzburger, M., Ju, L., Duda, M., & Skamarock, W. (2011). Exploring a Multiresolution
 1216 Modeling Approach within the Shallow-Water Equations. *Monthly Weather Review*, 39, 3348-3368.
 1217 <https://doi.org/10.1175/MWR-D-10-05049.1>
- 1218 Rodwell, M.J., & Hoskins, B.J. (1996). Monsoons and the dynamics of deserts. *Quarterly Journal of the Royal*
 1219 *Meteorological Society*, 122, 1385-1404. <https://doi.org/10.1002/qj.49712253408>
- 1220 Rummukainen, M. (2015). Added value in regional climate modeling. *Wiley Interdisciplinary Reviews: Climate*
 1221 *Change*, 7(1), 145–159. <https://doi.org/10.1002/wcc.378>
- 1222 Schmidt, G., Bader, D., Donner, L., Elsaesser, G., Golaz, J.-C., Hannay, C. et al.(2017). Practice and philosophy of
 1223 climate model tuning across six US modeling centers. *Geoscientific Model Development*, 10, 3207-3223.
 1224 <https://doi.org/10.5194/gmd-10-3207-2017>
- 1225 Sen, O., Ezber, Y., & Bozkurt, D. (2019). Euro-Mediterranean climate variability in boreal winter: a potential role of
 1226 the East Asian trough. *Climate Dynamics*, 52. <https://doi.org/10.1007/s00382-018-4573-9>
- 1227 Simpson, I., Seager, R., Shaw, T., & Ting, M. (2015). Mediterranean Summer Climate and the Importance of
 1228 Middle East Topography. *Journal of Climate*, 28, 1977-1996. <https://doi.org/10.1175/JCLI-D-14-00298.1>
- 1229 Small, R. J., Bacmeister, J., Bailey, D., Baker, A., Bishop, S., Bryan, F., et al. (2014). A new synoptic-scale
 1230 resolving global climate simulation using the Community Earth System Model. *Journal of Advances in Modeling*
 1231 *Earth Systems*, 6. <https://doi.org/10.1002/2014MS000363>
- 1232 Song, X., & Yu, L. (2017). Air-Sea heat flux climatologies in the Mediterranean Sea: Surface energy balance and its
 1233 consistency with ocean heat storage. *Journal of Geophysical Research: Oceans*, 122.
 1234 <https://doi.org/10.1002/2016JC012254>
- 1235 Taylor, M. A., & Fournier, A. (2010). A compatible and conservative spectral element method on unstructured
 1236 grids. *Journal Of Computational Physics*, 229, 5879-5895. <https://doi.org/10.1016/j.jcp.2010.04.008>
- 1237 Tomita, H. (2008). A Stretched Icosahedral Grid by a New Grid Transformation. *Journal of the Meteorological*
 1238 *Society of Japan*, 107-119. <https://doi.org/10.2151/jmsj.86A.107>
- 1239 Toreti, A., Xoplaki, E., Maraun, D., Kuglitsch, F. G., Wanner, H., & Luterbacher, J. (2010). Characterisation of
 1240 extreme winter precipitation in Mediterranean coastal sites and associated anomalous atmospheric circulation
 1241 patterns. *Natural Hazards and Earth System Sciences*. <https://doi.org/10.5194/nhess-10-1037-2010>
- 1242 Tuel, A., & Eltahir, E. A. B. (2021). Mechanisms of European Summer Drying under Climate Change. *Journal of*
 1243 *Climate*, 34, 8913–8931. <https://doi.org/10.1175/JCLI-D-20-0968.1>
- 1244 Tyrlis, E., & Lelieveld, J. (2013). Climatology and Dynamics of the Summer Etesian Winds over the Eastern
 1245 Mediterranean. *Journal of the Atmospheric Sciences*, 70, 3374–3396. <https://doi.org/10.1175/JAS-D-13-035.1>

- 1246 Ullrich, P. (2014). Squadgen: Spherical quadrilateral grid generator. University of California, Davis, Climate and
 1247 Global Change Group software.[Available online at <http://climate.ucdavis.edu/squadgen.php>.]
- 1248 Van Kampenhout, L., Rhoades, A., Herrington, A., Zarzycki, C., Lenaerts, J., Sacks, W., & Van den Broeke, M.
 1249 (2019). Regional grid refinement in an Earth system model: impacts on the simulated Greenland surface mass
 1250 balance. *The Cryosphere*, 13, 1547-1564. <https://doi.org/10.5194/tc-13-1547-2019>
- 1251 Vautard, R., Yiou, P., D'Andrea, F., de Noblet, N., Viovy, N., Cassou, C., et al. (2007). Summertime European heat
 1252 and drought waves induced by wintertime Mediterranean rainfall deficit. *Geophysical Research Letters*, 34.
 1253 <https://doi.org/10.1029/2006gl028001>
- 1254 Wang, Y., Leung, L., McGregor, J., Lee, D.-K., Wang, W.-C., Ding, Y., & Kimura, F. (2004). Regional Climate
 1255 Modeling: Progress, Challenges, and Prospects. *Journal of The Meteorological Society of Japan*, 8, 1599-1628.
 1256 <https://doi.org/10.2151/jmsj.82.1599>
- 1257 Wang, M., Ullrich, P., & Millstein, D. (2020). Future projections of wind patterns in California with the variable-
 1258 resolution CESM: a clustering analysis approach. *Climate Dynamics*, 54, 2511–2531.
 1259 <https://doi.org/10.1007/s00382-020-05125-5>
- 1260 Wentz, F.J., Meissner, T., Gentemann, C., Hilburn, K.A., & Scott, J. (2014) Remote Sensing Systems GCOM-W1
 1261 AMSR2 [Monthly] Environmental Suite on 0.25 deg grid, Version v08.2. Remote Sensing Systems, Santa Rosa,
 1262 CA. Available online at www.remss.com/missions/amr. [Accessed 20 July 2023].
- 1263 Wijngaard, R., Herrington, A., Lipscomb, W., Leguy, G., & An, S.-I. (2023). Exploring the ability of the variable-
 1264 resolution CESM to simulate cryospheric-hydrological variables in High Mountain Asia. *The Cryosphere*.
 1265 <https://doi.org/10.5194/tc-2022-256>
- 1266 Williamson, D. L. (2013). The effect of time steps and time-scales on parametrization suites. *Quarterly Journal of*
 1267 *the Royal Meteorological Society*, 139(671), 548–560. <https://doi.org/10.1002/qj.1992>
- 1268 Wu, C., Liu, X., Lin, Z., Rhoades, A. M., Ullrich, P. A., Zarzycki, C. M., Lu, Z., & Rahimi-Esfarjani, S.
 1269 R. (2017). Exploring a variable-resolution approach for simulating regional climate in the Rocky Mountain region
 1270 using the VR-CESM. *Journal of Geophysical Research: Atmospheres*, 122, 10,939–
 1271 10,965. <https://doi.org/10.1002/2017JD027008>
- 1272 Xie, S., Lin, W., Rasch, P. J., Ma, P. L., Neale, R., Larson, et al. (2018). Understanding cloud and convective
 1273 characteristics in version 1 of the E3SM atmosphere model. *Journal of Advances in Modeling Earth*
 1274 *Systems*, 10, 2618–2644. <https://doi.org/10.1029/2018MS001350>
- 1275 Xie, P., Yatagai, A., Chen, M., Hayasaka, T., Fukushima, Y., Liu, C., & Yang, S. (2007) A gauge-based analysis of
 1276 daily precipitation over East Asia. *Journal of Hydrometeorology*, 8, 607–626. <https://doi.org/10.1175/JHM583.1>
- 1277 Xoplaki, E. (2002) *Climate variability over the Mediterranean* (PhD thesis). University of Bern, Switzerland.
- 1278 Zarzycki, C., Jablonowski C., & Taylor, M. A. (2014). Using variable-resolution meshes to model tropical cyclones
 1279 in the Community Atmosphere Model. *Monthly Weather Review*, 142, 1221–1239. <https://doi.org/10.1175/MWR-D-13-00179.1>
- 1281 Zarzycki, C., Jablonowski, C., Thatcher, D., & Taylor, M. (2015). Effects of Localized Grid Refinement on the
 1282 General Circulation and Climatology in the Community Atmosphere Model. *Journal of Climate*, 28,
 1283 150119122716002. <https://doi.org/10.1175/JCLI-D-14-00599.1>
- 1284 Zarzycki, C., Levy, M. N., Jablonowski, C., Overfelt, J. R., Taylor, M. A., & Ullrich, P. A. (2014). Aquaplanet
 1285 experiments using CAM's variable-resolution dynamical core. *Journal of Climate*, 27(14), 5481–5503.
 1286 <https://doi.org/10.1175/JCLI-D-14-00004.1>